J. Fluid Mech. (1993), *vol.* 249, *pp.* 465–498

A Reynolds stress model for near-wall turbulence

By P. A. DURBIN

Center for Turbulence Research, Stanford University, Stanford, CA 94305-3030, USA

(Received 28 April 1992 and in revised form 22 August 1992)

A tensorially consistent near-wall second-order closure model is formulated. Redistributive terms in the Reynolds stress equations are modelled by an elliptic relaxation equation in order to represent strongly non-homogeneous effects produced by the presence of walls; this replaces the quasi-homogeneous algebraic models that are usually employed, and avoids the need for *ad hoc* damping functions. A quasi-homogeneous model appears as the source term in the elliptic relaxation equation – here we use the simple Rotta return to isotropy and isotropization of production formulae. The formulation of the model equations enables appropriate boundary conditions to be satisfied.

The model is solved for channel flow and boundary layers with zero and adverse pressure gradients. Good predictions of Reynolds stress components, mean flow, skin friction and displacement thickness are obtained in various comparisons to experimental and direct numerical simulation data.

The model is also applied to a boundary layer flowing along a wall with a 90°, constant-radius, convex bend. Because the model is of a general, tensorially invariant form, special modifications for curvature effects are not needed; the equations are simply transformed to curvilinear coordinates. The model predicts many important features of this flow. These include: the abrupt drop of skin friction and Stanton number at the start of the curve, and their more gradual recovery after the bend; the suppression of turbulent intensity in the outer part of the boundary layer; a region of negative (counter-gradient) Reynolds shear stress; and recovery from curvature in the form of a Reynolds stress 'bore' propagating out from the surface. A shortcoming of the present model is that it overpredicts the rate of this recovery.

A heat flux model is developed. It is shown that curvature effects on heat transfer can also be accounted for automatically by a tensorially invariant formulation.

1. Introduction

Transport of heat and momentum to a surface beneath a turbulent boundary layer is controlled largely by a region immediately next to the surface. The proximate boundary suppresses the normal component of turbulent intensity within this region (Hunt & Graham 1978), thereby reducing mixing and making the near-wall region one of high impedance to heat and momentum transfer between the boundary and fluid. By 'near-wall', we are referring to what is called the law-of-the-wall layer in a zero-pressure-gradient boundary layer. It is where the turbulent kinetic energy is maximum and is the primary area of turbulence production; in every respect, it is a crucial portion of the turbulent boundary layer. However, this near-wall region has proven rather an anathema to turbulence modellers.

The objective of near-wall turbulence closure modelling is to formulate a set of differential equations which can be solved for single-point turbulence statistics in a region of the flow which extends to the wall and includes the crucial law-of-the-wall layer. Boundary conditions to the model are then imposed at the wall. This is in contrast to the 'wall function' approach, in which boundary conditions are replaced by matching conditions to a logarithmic layer – hence, assuming that the logarithmic layer exists and has a universal form and, implicitly, that the law-of-the-wall region is also universal. The objective of the near-wall model is to be more flexible, and not to require any such assumption of universal behaviour. In many non-equilibrium flows, such as a boundary layer subjected to a large pressure gradient or to substantial surface curvature, the near wall-turbulence is not of a universal form.

The distinctive features of turbulence in the region immediately adjacent to a smooth surface are strong inhomogeneity and large anisotropy. Virtually all previous models for the near-wall region have used isotropic or quasi-homogeneous assumptions in some significant aspect of their formulation. Such formulations produce solutions which are strikingly at odds with experiment – as could be expected. So-called 'damping functions' are then introduced to correct this erroneous behaviour of the basic model (Patel, Rodi & Scheurer 1985; Hanjalic & Launder 1976). The damping function adjusts the model solution to fit a particular data set; but by its nature, it removes the flexibility that the differential equations of the model were meant to provide: essentially, the assumption of a universal damping function is analogous to the universality invoked in the wall function method. The failure of the universal wall-layer assumption is illustrated by Rodi & Scheurer (1986): they show how a damping function which fits a model to zero-pressure-gradient boundary-layer data gives incorrect behaviour in an adverse pressure gradient. In consequence of having examined both these quasi-homogeneous or isotropic types of model, and a wealth of near-wall direct numerical simulation (DNS) data (Mansour, Kim & Moin (1988), it seems clear that the substantial corrections which damping functions must make are required because the models have neglected crucial aspects of inhomogeneity and anisotropy of the near-wall turbulence. While it may not be obvious how these aspects can be represented by model differential equations, attempts in that direction certainly are warranted. The present paper is part of a research programme in which we eschew the damping function route, and instead attempt to incorporate near-wall effects of inhomogeneity and anisotropy into the governing equations.

The original basis of our approach is set out in Durbin (1991), upon which we rely heavily. That paper describes a version of the model which uses an eddy viscosity for mean momentum transport (the k–ϵ–$\overline{v^2}$ version). It was applied to boundary layers and heat transfer in Durbin (1992). The present paper develops a full, tensorially invariant, Reynolds stress closure. The simpler version produced excellent results in channel and boundary-layer flow, including moderate adverse pressure gradients; however, when the pressure rise of the adverse pressure gradient is sufficient to drive the skin friction near to zero, the eddy-viscosity approximation causes the boundary layer to grow too rapidly, as will be illustrated here. Presumably this is because the eddy-viscosity approximation ignores the effect of upstream history upon the Reynolds shear stress. By carrying a differential equation for Reynolds shear stress we obtain considerably better results for the adverse-pressure-gradient boundary layer with large pressure rise.

Another advantage of the coordinate-independent Reynolds stress closure is that it can be applied to non-planar boundary layers. Here we present computations of a boundary layer on a convexly curved surface. Surface curvature has a pronounced effect on attached turbulent boundary layers. Bradshaw (1973) reviews the history of the subject: it appears that, about 1930, Prandtl deduced theoretically that curvature would have a disproportionately *small* effect. However, this deduction was promptly disproved by his student, Wilcken, who showed experimentally that the effect was disproportionately *large*. A coefficient in a modified mixing-length formula which Prandtl had inferred to be $\frac{1}{4}$ was found experimentally to be more than a factor of 10 larger (Johnston 1978).

If R_c is the surface radius of curvature and δ the 99% thickness of the boundary layer, then $\delta/R_c \geqslant 0.05$ is considered to be strong curvature (Gillis *et al.* 1980). The smallness of this parameter is misleading: the relevant comparison is between the rates of curvature and shear production of turbulent kinetic energy, which is characterized by $\delta U_\infty/R_c u_*$ in law-of-the-wake scaling; under strong curvature this parameter is $O(1)$. In law-of-the-wall scaling, the ratio of curvature to shear is of order $\nu/R_c u_*$, which is small in high-Reynolds-number flow. Thus, curvature has insignificant *direct* effect on the viscous wall layer; but it does have a significant *indirect* effect through the communication between the wall and outer regions. For instance, the skin friction falls abruptly as a boundary layer enters a region of strong convex curvature, even though skin friction is a viscous effect.

Other effects of strong convex curvature include: suppression of turbulent intensity throughout the boundary layer, although most notably in the outer half; decrease of the Reynolds shear stress, to the extent that in the outer half of the layer it can be driven negative, producing 'counter-gradient' transport; and an apparent reorganization of the boundary-layer turbulence, which persists in the flat-plate boundary layer downstream of a curved section (Gillis *et al.* 1980). The persistent effects include lowered skin friction, which led Bushnell (1983) to propose that convex curvature might be a practical means of drag reduction. These characteristic features of convex curvature make the curved-wall turbulent boundary layer an intriguing flow to compute with a turbulence model.

Mathematically, the effects of curvature are described by metric terms in the governing equations of motion – or, strictly, these metric terms and the assumption that the boundary layer remains attached. (The assumption of attached flow is the Occam's razor of boundary-layer theory: if the boundary-layer solution is not singular, it is supposed that the flow remains attached.) The metric terms couple components of the Reynolds stress tensor: for example, the curvature term in the $\overline{v^2}$-equation is proportional to $\overline{uv}$. Simplified models, such as mixing length or $k-\epsilon$, which contain no explicit representation of the turbulence anisotropy cannot automatically account for the effects of curvature; if such effects are to be included they must be added *ex post facto*. By contrast, Reynolds stress models have the potential to account for curvature without requiring any modification to their equations.

Metric terms also enter the equations for the heat-flux tensor $-\overline{u_i\theta}$; they couple the $\overline{u\theta}$ and $\overline{v\theta}$ equations. Again this produces a curvature effect which is not included in simple models, such as eddy diffusion. We will formulate a Reynolds heat-flux model, so that curvature effects again arise naturally from transformation of the coordinate system. The explicit curvature terms in the heat-flux equations are additional to the implicit effects due to curvature in the Reynolds stress equations. Thus, curvature affects heat transfer both indirectly, by modifying turbulent convective transport, and directly by 'Coriolis' terms which interchange x- and y-components of heat flux.

2. The model

The exact Reynolds stress transport equation can be written

$$D_t\overline{u_iu_j} = \wp_{ij} + P_{ij} - \frac{\overline{u_iu_j}}{k}\epsilon - \partial_k\overline{u_ku_iu_j} - \frac{2}{3\rho}\delta_{ij}\partial_k\overline{u_kp} + \nu\nabla^2\overline{u_iu_j}, \tag{1}$$

where

$$P_{ij} = -\overline{u_iu_k}\partial_k U_j - \overline{u_ju_k}\partial_k U_i \tag{2}$$

is the rate of turbulence production by mean velocity gradients,

$$\wp_{ij} = -\frac{1}{\rho}\overline{u_i\partial_jp} - \frac{1}{\rho}\overline{u_j\partial_ip} + \frac{2}{3\rho}\delta_{ij}\partial_k\overline{u_kp} - \epsilon_{ij} + \frac{\overline{u_iu_j}}{k}\epsilon \tag{3}$$

is the redistribution tensor; and $D_t(\cdot)$ is the convective derivative following the mean flow. Note that the Rotta model for anisotropic dissipation, $-\overline{u_iu_j}\epsilon/k$, has been added to (1) and subtracted from (3): among other virtues, this has the effect of making $\wp_{ij}$ vanish at rigid, no-slip boundaries. By definition $\epsilon = \frac{1}{2}\epsilon_{ii}$ is the rate of dissipation of turbulent kinetic energy (k). The 'pressure transport', $-\partial_k\overline{u_kp}$, has also been added to (1) and subtracted from (3): this is done to make (3) redistributive.

In the notation of (3) all unclosed terms have been incorporated into $\wp_{ij}$, except for the transport terms. We follow the usual practice of modelling turbulent self-transport by gradient diffusion (Launder 1989):

$$-\partial_l\overline{u_lu_iu_j} = \partial_l\left(\frac{\nu_{T_{lm}}}{\sigma_k}\partial_m\overline{u_iu_j}\right). \tag{4}$$

This amounts to regarding $\overline{u_iu_j}$ as a 'substance' being transported by the turbulent velocity u_l. The diffusional model is as much a representation of the smoothing effect of ensemble averaging as of convective transport *per se*: this is why the model is parabolic rather than hyperbolic. For the eddy viscosity

$$\nu_{T_{ij}} = C_\mu\overline{u_iu_j}T \tag{5}$$

will be used. In (4) we follow the convention of writing the eddy viscosity for turbulent transport of Reynolds stress in the form ν_T/σ_k, where σ_k is a constant Prandtl number. For the timescale T we adopt (Durbin 1991)

$$T = \max\left(\frac{k}{\epsilon}, C_T\left(\frac{\nu}{\epsilon}\right)^{\frac{1}{2}}\right). \tag{6}$$

This becomes k/ϵ far from boundaries. Near a surface where $k\rightarrow 0$ it becomes the Kolmogoroff timescale $C_T(\nu/\epsilon)^{\frac{1}{2}}$, which is a suitable lower bound on T. The pressure transport term in (1) and (3) is usually small (Mansour *et al.* 1988) and will be set to zero; a frequently given justification for dropping this term is that it is assumed to be absorbed into the transport model (4).

A second-order closure for $\wp_{ij}$ is simply a proposed relationship between this unknown and the dependent variable of equation (1), $\overline{u_iu_j}$. In all closures to date, this relationship has consisted of algebraic formulae. However, those formulae are based on quasi-homogeneous assumptions – most notably in the rapid pressure–strain term–which are incorrect in the strongly inhomogeneous near-wall region (Bradshaw, Mansour & Piomelli 1987). It is suggested in Durbin (1991) that elliptic effects within the flow, which are caused by the proximity of a boundary, might be included by formulating an elliptic relaxation model for $\wp_{ij}$. The elliptic effects are blocking of the normal velocity (the 'image vortex' effect: Hunt & Graham 1978) and pressure reflection from the surface. Because these are inherently non-local effects, which cannot appear explicitly in any single-point model, they are represented quite indirectly by the present model.

Occasionally, wall effects have been introduced by using the unit wall normal explicitly in formulae for turbulence properties interior to the fluid (Launder 1989). Of course, the wall normal is only defined at the wall, so this is an ambiguous procedure. An elliptic model provides a more natural way to let the wall effects appear: they enter through boundary conditions, and the model relaxes to quasi-homogeneous behaviour in the interior, far from the boundary. Wall effects then enter via solution at the governing equations, rather than via prescribed damping function profiles.

The elliptic relaxation model proposed by Durbin (1991) can be put into coordinate-independent form and written

$$\wp_{ij} = k f_{ij}, \tag{7}$$

$$L^2\nabla^2 f_{ij} - f_{ij} = -\Pi_{ij}. \tag{8}$$

The lengthscale L is formulated by analogy to (6):

$$L = C_L \max\left(\frac{k^{\frac{3}{2}}}{\epsilon}, C_\eta\left(\frac{\nu^3}{\epsilon}\right)^{\frac{1}{4}}\right). \tag{9}$$

(A word of caution: near the free-stream edge of a boundary layer, $\epsilon \rightarrow 0$ and the second factor in (9) can become large. For this reason, $L = C_L k^{\frac{3}{2}}/\epsilon$ should probably be used in place of (9) in the outermost regions of a boundary layer. However, (9) was used throughout the flow in the present computations, with no adverse effects.) Boundary conditions can be imposed on (8) to represent non-homogeneous effects of the wall. The boundary conditions influence the solution in the interior of the flow through the homogeneous solutions to (8). Far from the surface these solutions decay, and the f_{ij} relax to quasi-homogeneity, as represented by a balance of the second term on the left-hand side with the right-hand side.

An heuristic justification for (8), starting from the Poisson equation for pressure, is described in Appendix A. Ultimately, the motivation for (8) is simply a notion that non-local, elliptic effects – like kinematic blocking and pressure reflection – might indirectly be represented by an elliptic model equation. An exact representation of such processes would require knowledge of two-point correlations; this is why the real, fluid dynamical elliptic effects enter the present model indirectly at best.

The form (7) for $\wp_{ij}$ was introduced, making f_{ij} the dependent variable in (8), in order to enforce the condition $\wp_{ij}(0) = 0$. The factor of k causes $\overline{v^2}$ to be of order y^4 as $y \rightarrow 0$ – see §3 and Durbin (1991).

In the quasi-homogeneous limit (7) and (8) reduce to

$$\wp_{ij} = k\Pi_{ij}. \tag{10}$$

For Π_{ij} any quasi-homogeneous model can be used. Here we adopt the simple model recommended by Launder (1989). This consists of a sum of Rotta's return to isotropy and the isotropization of production models:

$$\Pi_{ij} = \frac{1-C_1}{kT}\left(\overline{u_i u_j} - \tfrac{2}{3}k\delta_{ij}\right) - \frac{C_2}{k}\left(P_{ij} - \tfrac{2}{3}P\delta_{ij}\right), \tag{11}$$

where $2P = P_{ii}$, and P_{ij} is given by (2). C_1 is the usual Rotta constant. The last two terms of (3) require that unity be subtracted from C_1 as in (11). Far from the surface, the model for $\wp_{ij}$ then relaxes to a quasi-homogeneous form with C_1 appearing as the standard Rotta constant and ϵ_{ij} replaced by the isotropic form $2/3\delta_{ij}\epsilon$.

One half the trace of (1) (obtained by setting $i = j$ and summing) is the kinetic energy equation:

$$D_t k = P - \epsilon + \partial_l \left(\nu \delta_{lm} + \frac{\nu_{\mathrm{T}lm}}{\sigma_k} \right) \partial_m k, \tag{12}$$

which may be solved in place of one of equations (1). As mentioned previously, $1/\rho\, \partial_i (\overline{u_i p})$ was omitted – or absorbed into the eddy diffusive transport – in (12).

Equation (12) is not coupled to an elliptic equation; however, it is coupled to an equation for ϵ, again forming a fourth-order system of equations. We adopt the standard ϵ-model (Patel *et al.* 1985)

$$D_t \epsilon = \frac{C^*_{\epsilon_1} P - C_{\epsilon_2} \epsilon}{T} + \partial_k \left(\nu \delta_{kl} + \frac{\nu_{\mathrm{T}kl}}{\sigma_\epsilon} \right) \partial_l \epsilon. \tag{13}$$

Here $C^*_{\epsilon_1} = C_{\epsilon_1}(1 + a_1 P/\epsilon)$ was made a function of P/ϵ to account for the anisotropic production terms in the near wall region (Durbin 1992; Durbin & Speziale 1991); otherwise the constants have their usual meanings. The system of equations (12) and (13) is subject to the no-slip condition $k = \partial_y k = 0$ on boundaries, where y denotes the direction normal to the surface. Note that we do not need boundary conditions on ϵ: the conditions on k and its normal derivative are sufficient to obtain both k and ϵ by solving the fourth-order system, (12) and (13).

Values of the model constants are quite similar to those given in Patel *et al.* (1985), Launder (1989) and Durbin (1992). Thus, for the k–ϵ system (12) and (13) with (6)

$$C_{\epsilon_1} = 1.44; \quad C_{\epsilon_2} = 1.9; \quad \sigma_k = 1.2; \quad \sigma_\epsilon = 1.65; \quad C_\mu = 0.23; \quad a_1 = 0.1 \tag{14a}$$

are used. The constants appearing in the length and time scales T and L are set to

$$C_T = 6.0; \quad C_L = 0.2; \quad C_\eta = 80.0. \tag{14b}$$

The primary purpose for using the Kolmogoroff scale as a lower bound on T in (6) is to avoid a singularity at $y = 0$ in the first term on the right-hand side of (13). The value of $C_T = 6$ was determined in Durbin (1991) by reference to DNS data, and shown to produce the correct behaviour of ϵ near a wall. The other constants were determined by comparing model predictions of the normal component of turbulent intensity $(\overline{v^2})$ to data. The constants in (11) are chosen as

$$C_1 = 1.22; \quad C_2 = 0.6. \tag{14c}$$

The second constant is set to the standard value derived from perturbation of isotropy (Launder 1989). The first is a bit lower than usual for the Rotta return to isotropy constant. Experiments on the rate of return to isotropy do not provide a unique value (Lumley & Newman 1977); indeed, as the turbulence tends toward two-dimensionality, C_1 tends toward unity. Near-wall turbulence tends toward two-dimensionality as the surface is approached, so the slower rate of return implied by (14*c*) is not unwarranted. Indeed, it has been suggested that C_1 be made a function of the invariants of the Reynolds stress tensor that becomes unity in two-component turbulence: the value of unity is suggested by realizability constraints (Lumley & Newman 1977).

In computations not shown here C_1 was set to 1.5 and a_1 to 0.05. These values are more consistent with those used in free-shear layer models. The agreement between experiment and model was only slightly worse than that shown here; 1.5 and 0.05 are satisfactory values. Clearly, leeway exists for reaching a compromise between wall-bounded and free-shear flows.

3. Boundary conditions

Boundary conditions to the model equations are derived from an examination of the near-wall behaviour of their solutions. The no-slip condition causes k to tend to $\epsilon y^2/2\nu$ as $y \rightarrow 0$. By its definition (3) and no-slip at the wall, $\wp_{ij}$ is $O(y)$. If the pressure transport term is omitted and i and j are both in the normal direction, $\wp_{ij}$ will be $O(y^2)$. It follows that in the viscous layer immediately next to the wall, the dominant balance of terms in (1) is

$$\nu\partial_y^2\overline{u_i u_j} - 2\nu\frac{\overline{u_i u_j}}{y^2} = O(y). \tag{15}$$

This represents a balance between molecular diffusion and anisotropic dissipation. The solution to (15) is

$$\overline{u_i u_j} = A_{ij}y^2 + B_{ij}/y + O(y^3),$$

where A_{ij} and B_{ij} are integration constants determining the magnitude of homogeneous solutions to the differential equation. The no-slip condition causes tangential velocity components to go to zero like $O(y)$, while the normal component is $O(y^2)$, by continuity. Hence, if i or j correspond to the normal direction $\overline{u_i u_j} = o(y^2)$, so the proper boundary condition is to require

$$A_{ij} = B_{ij} = 0, \quad i \text{ or } j \text{ in normal direction.} \tag{16}$$

If i and j both correspond to tangential directions, then $\overline{u_i u_j} = O(y^2)$, so only

$$B_{ij} = 0, \quad i \text{ and } j \text{ in tangential direction} \tag{17}$$

is required of (1). Equations (1) and (8) provide a fourth-order system of equations for each $\overline{u_i u_j}$. Thinking of flow in a channel with two boundaries, one sees that (16) applied at each wall gives the appropriate number of boundary conditions (that is, four conditions for the fourth-order system). For tangential components, a condition additional to (17) is required at each wall. At present, that additional condition is somewhat uncertain. From the numerical computations described later, we surmise that $f_{ij} = 0$ for i and j tangential may often be the appropriate condition; however, this matter must be discussed further.

Consider first the k–ϵ system of equations, (12) and (13). This system requires four boundary conditions. The no-slip condition $k = \partial_y k = 0$ at the walls of a channel imposes all four conditions on k. The surface value of ϵ floats to whatever value is required. Indeed, it is a rather remarkable property of the ϵ-equation that, when solved in this manner, it produces a sharp rise in ϵ near the wall, with a peak at the wall, in agreement with DNS data. The magnitude and Reynolds-number dependence of this peak are reproduced quite reasonably by the model (Durbin 1991).

Similarly, because each $\overline{u_i u_j} - \wp_{ij}$ pair of equations forms a coupled, fourth-order system, four conditions imposed on $\overline{u_i u_j}$ make their solution determinate. With $B_{ij} = 0$ and A_{ij} specified at the boundaries, the value of f_{ij} at the wall and the homogeneous solutions to (8) would be determined implicitly by the solution to the complete set of model equations. The application of boundary conditions (16) to the systems of equations for $\overline{uv}$ and $\overline{v^2}$ in channel flow is a case in point: the homogeneous solutions to (8) are determined implicitly by the process of solving the model equations with boundary conditions only on the velocities – as was discussed in the preceding paragraph. It will be found in the next section that, in this manner, conditions (16) produce eminently reasonable results. As explained in Durbin (1991), the homogeneous solution to (8) counteracts the particular solution, forced by its right-hand side, thereby modelling the blocking effect of the wall.

However, there is no means for prescribing tangential components such as A_{11}; in fact A_{11} is equal to $\epsilon_{11}/2\nu$ evaluated at the wall. This cannot be prescribed *a priori*. If A_{11} were prescribed, the homogeneous solutions to the f_{11}-equation would again counteract the particular solution, causing an erroneous blocking effect on the tangential component; blocking should only suppress the normal component. A suitable condition seems to be that $f_{11} = 0$ at the wall; this condition causes the homogeneous solution of (8) to vanish, thus avoiding spurious suppression of the tangential component. As will be seen, this boundary condition in conjunction with (17) produces a satisfactory solution for $\overline{u^2}$. The solution for $\overline{w^2}$, as found from $\overline{w^2} = 2k - \overline{u^2} - \overline{v^2}$, will also be found satisfactory.

In general the k-equation and only two of the diagonal components of the Reynolds stress equations need be solved. Thus, the above considerations on boundary conditions suffice to make the model solutions determinate. However, those observations give rise to a slight dilemma: the contraction of the modelled form of (1) must give the k-equation (12). This requires that the contraction of $\wp_{ij}$ vanish. The model (11) was formulated so that it contracts to 0; hence (8) contracts to

$$L^2\nabla^2 f_{ii} - f_{ii} = 0.$$

The solution to this will be identically zero, as required in the k-equation, if $f_{ii} = 0$ on the boundaries. Since $f_{11} = 0$ appears to be a suitable boundary condition, the implication is that $f_{33} = -f_{22}$ would be the boundary condition on the $\overline{u_3 u_3}$–$\wp_{33}$ system of equations. Thus, the tangential condition seems not to be as simple as setting $f_{ij} = 0$ for i and j tangential. This is a puzzle which at present we cannot solve; nor need we, because the $\overline{u_3 u_3}$ equation will not be used. Since $\overline{v^2}$ is small near the wall, and blocking effects do not occur in the k- or $\overline{u^2}$-equations, it would seem that the present formulation will not cause spurious blocking of $\overline{w^2}$. Hence, the dilemma just cited is one of principle, but it causes no practical difficulty.

4. Calculations of channel flow and flat-plate boundary layers

The ideal flow for developing a near-wall turbulence model is the two-dimensional channel flow: this flow is statistically homogeneous in planes parallel to the walls, so the turbulence statistics are functions of the cross-stream coordinate y alone. A wealth of numerical and experimental data are available for this flow. The constants for the present model were determined by comparing numerical solutions of the model equations to DNS data of Dr J. Kim (1990, private communication). These DNS data were computed in a channel with Reynolds number based on friction velocity and channel half-height equal to 395. We will also present results for two-dimensional boundary layers. In both cases the model equations were solved by a semi-implicit, parabolic marching scheme; in the channel this marching converged to the steady-state solution. The boundary-layer equations were obtained by the usual procedure of consistently dropping x-derivatives of a given quantity in comparison to y-derivatives of that quantity.

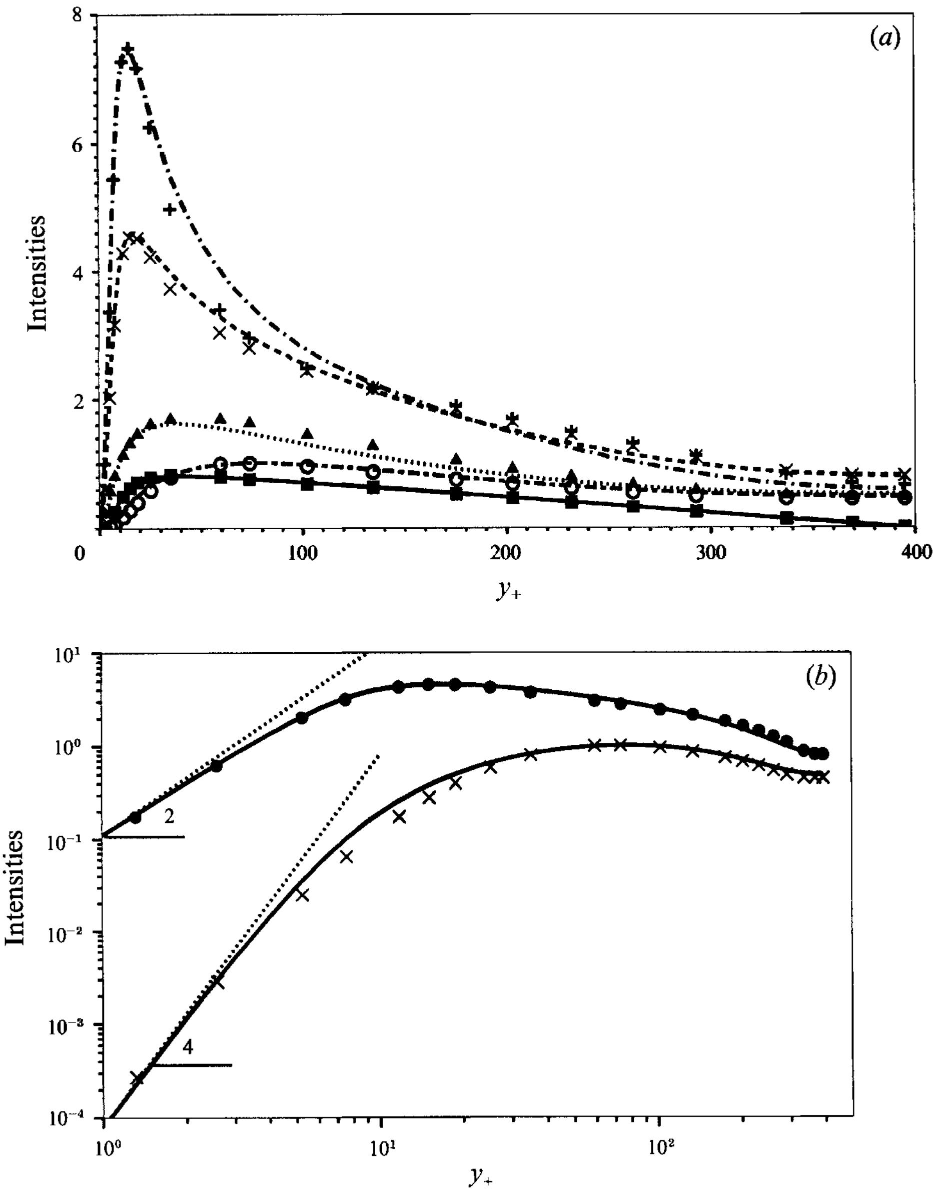

FIGURE 1. (*a*) Comparison of model (lines) to DNS (symbols) profiles of Reynolds stresses in channel flow at $R_\tau = 395$: +, $\overline{u^2}$; ×, k; ▲, $\overline{w^2}$; ○, $\overline{v^2}$; ■, $-\overline{uv}$. (*b*) The behaviour adjacent to the wall, and the y^2 and y^4 asymptotic limits: ●, k; ×, $\overline{v^2}$.

The $\overline{u_1 u_1}$, $\overline{u_2 u_2}$ and $\overline{u_1 u_2}$-components of (1) were solved, while the last, $\overline{u_3 u_3}$, component was determined from the definition $2k = \overline{u_i u_i}$, into which the solutions for k and the other two normal stress components were substituted.

Figure 1 shows a numerical solution to the model for channel flow at a friction-velocity Reynolds number of $R_\tau = 395$. The four non-zero components of the Reynolds stress tensor and the kinetic energy are shown. The model solution is represented by the curves and DNS data provided by Dr J. Kim (private communication) are shown by the symbols. Wall units are used so the turbulent intensities are normalized by the

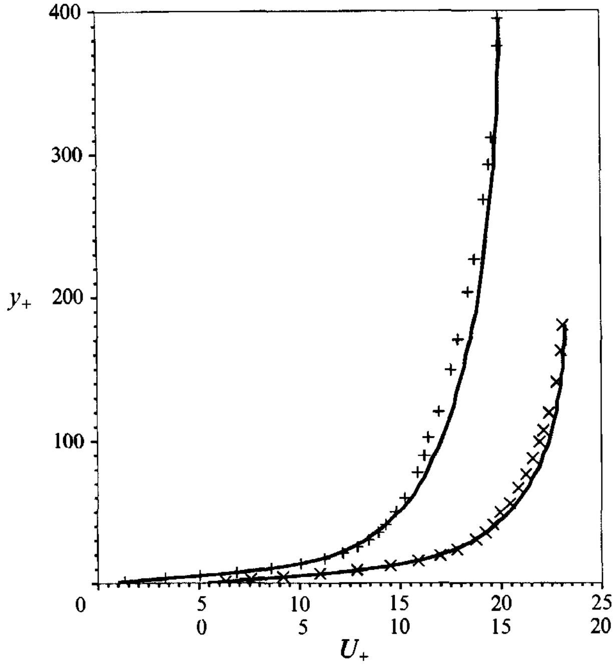

FIGURE 2. Mean velocity profiles in wall units, DNS data: ×, $R_\tau = 180$; +, $R_\tau = 395$. The profile for $R_\tau = 180$ has been displaced by 5 units for legibility.

kinematic wall stress, u_*^2, and the y-coordinate by ν/u_*. It is seen that in the near-wall region, $y_+ < 100$, all components of the Reynolds stress tensor behave correctly: this includes the peaking of $\overline{u^2}$ and k, the suppression of $\overline{v^2}$ for $y_+ < 40$ and the rise of $-\overline{uv}$ to its maximum at about $y_+ = 40$. The maximum of $-\overline{uv}$ is less than unity due to the smallness of the Reynolds number. In figure 4, for a boundary layer at considerably higher Reynolds number, it will be seen that $-\overline{uv}$ reaches a maximum value of unity. Hence, one sees that suitable Reynolds-number dependence is captured by the model without introducing any such dependence explicitly into its coefficients; the Reynolds-number dependence comes from the exact viscous terms. At the largest values of y_+, corresponding to the central portion of the channel, $\overline{u^2}$ falls below the data, although the other components are in reasonable agreement with the data. A similar level of agreement to that shown by figure 1 was obtained at the lower value $R_\tau = 180$, although the tendency of $\overline{u^2}$ to fall too low at the centre of the channel was exacerbated.

In the lower portion of figure 1(*b*), k and $\overline{v^2}$ are shown on logarithmic axes so that their approach to the limiting y_+^2 and y_+^4 forms can be seen. This figure illustrates how the numerical solution is consistent with the analysis in §3.

Figure 2 shows mean flow profiles at both $R_\tau = 180$ and 395. The value of U_+ at the largest y_+, which corresponds to the centre of the channel, determines the skin-friction coefficient. The model predicts this coefficient and its Reynolds-number dependence quite well. The mean velocity profile shows some discrepancy with the data for y_+ around 100, corresponding to the logarithmic region, but is generally of reasonable form. The log-law plays no direct role in the present model because the equations are solved to the surface; hence the small differences between model and data in the logarithmic region are not crucial. The simplified model of Durbin (1992) fitted the logarithmic region quite well.

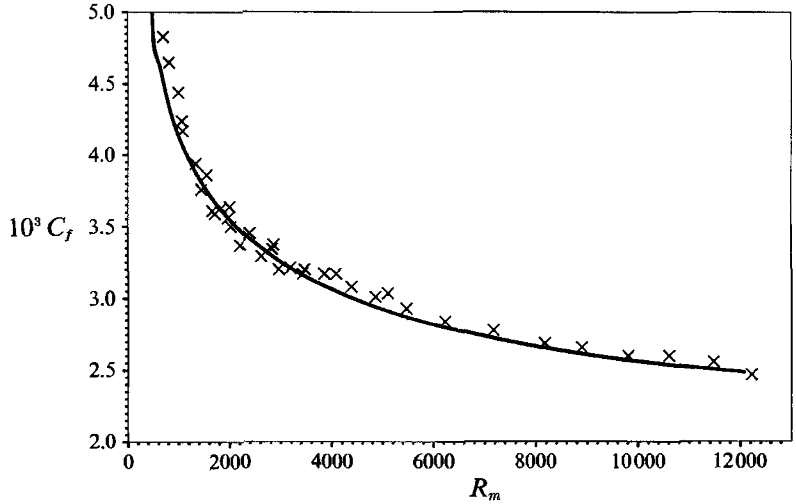

FIGURE 3. Friction coefficient in a zero-pressure-gradient boundary layer versus momentum-thickness Reynolds number. Experimental data is from Coles & Hirst; solid line is present model.

For flat-plate boundary layers, the mean x-momentum equation is

$$D_t U = -\frac{1}{\rho}\partial_x \mathscr{P} + \partial_y(\nu \partial_y U - \overline{uv}). \tag{18}$$

This is solved for a prescribed pressure distribution $\mathscr{P}(x)$, along with the continuity equation $\partial_x U + \partial_y V = 0$. Equation (18) requires a solution only to the $\overline{u_1 u_2}$-component of (1); however, P_{12} and Π_{12} contain $\overline{u_2^2}$, so the $\overline{u_2 u_2}$-component must also be solved. The boundary conditions to these equations are given in (16). For flat-plate boundary layers (12) and (13) are also solved; this provides a closed set of equations – there is no need to solve the other components of the Reynolds stress equation.

Free-stream boundary conditions are required for boundary-layer computations. It is widely known that k–ϵ, and similar transport equation models are erroneous in the outermost part of a boundary layer. The most obvious flaw is that they cause k to go to zero at some finite point (Kline *et al.* 1968, p. 327), instead of having a y^{-4} decay at large y. Because of this, we have followed the common pragmatism of allowing a small level of 'free-stream turbulence'. Thus, $k = 10^{-5} U_\infty^2$ is imposed at the topmost grid point. Computed results seem to be insensitive to this low level of free-stream turbulence. The other components of the Reynolds stress tensor at the free-stream are set by isotropy: $\overline{v^2} = \frac{2}{3}k$; $\overline{uv} = 0$. The rest of the free-stream boundary conditions were $\partial_y \epsilon = 0$, $\partial_y f_{11} = 0$ and $f_{12} = 0$ (these were also the conditions imposed by symmetry at the centreline of the previous channel flow case). Aside from using suitable free-stream conditions for the boundary layer, and suitable symmetry conditions at the channel centreline, the model, including values of the constants, was identical for all calculations.

Figure 3 shows model solutions for friction coefficient C_f versus momentum-thickness Reynolds number R_m in a zero-pressure-gradient boundary layer, compared to experimental data (Coles & Hirt 1968). The level of agreement is good, and similar to that obtained with the simpler k–ϵ–$\overline{v^2}$ version (Durbin 1992). It is quite significant that the correct Reynolds-number dependence has been predicted: this dependence arises largely through the exact viscous term in (1); the model contains no explicit functions of Reynolds number, so the result in figure 3 is an honest prediction of the

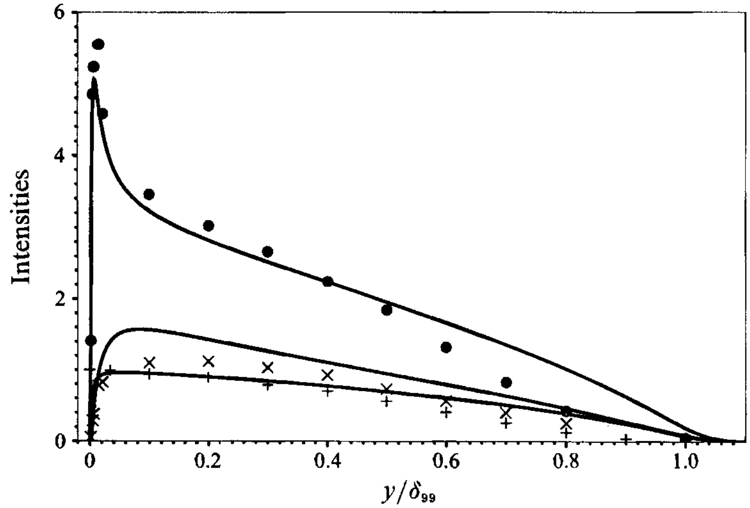

FIGURE 4. Profiles of k (●), $\overline{v^2}$ (×) and $-\overline{uv}$ (+) at $R_m = 7150$ in a zero-pressure-gradient boundary layer. Experimental data were transcribed from Klebanoff.

model. The Reynolds-number dependence is simply a property of the model equations. Although near-wall modelling is sometimes misleadingly referred to as 'low-Reynolds number modelling', in fact the Reynolds-number dependence arises in a natural way; the modelling has to address the issues of inhomogeneity and anisotropy.

Figure 4 shows k, $\overline{v^2}$ and $-\overline{uv}$ normalized by u_*^2, versus y/δ_{99}. The model solution and data from Klebanoff (1955) are for $R_m = 7150$; one sees that at this Reynolds number the normalized Reynolds shear stress reaches a maximum value of unity. $\overline{v^2}$ is somewhat overpredicted. In the simpler version of the model (Durbin 1992) $\overline{v^2}$ was more accurately predicted, but it also played a more essential role: there it determined the behaviour of the eddy viscosity in the mean momentum equation; here it influences the Reynolds shear stress through the production term in the $\overline{uv}$-equation. The kinetic energy has an appropriate, peaked form near the surface, although it is slightly below the data. k lies above the data in the outermost portion of the boundary layer.

The results so far show the viability of the present model; but as good results were obtained with the k–ϵ–$\overline{v^2}$ version. In the adverse-pressure-gradient boundary layer one begins to see an advantage to carrying a transport model for $-\overline{uv}$. Figure 5 shows results for the friction coefficient and displacement thickness in the Samuel & Joubert (1974) experiment on a boundary layer developing into an increasingly adverse pressure gradient. The friction coefficient is based on the upstream reference velocity and the displacement thickness is normalized on its value at the first measurement location; at that location $R_m = 4992$. $x - x_0$ is distance in metres downstream of the first measurement point. The data plotted in figure 5 come from table 1 of Samuel & Joubert. In Durbin (1992) it was found that the k–ϵ–$\overline{v^2}$ version gave excellent agreement with the skin-friction data. The displacement thickness was predicted very well for most of the range of x, but at the last measurement point it had risen above the data: where δ_*/δ_{*_0} in the data is just below 6, the model was just below 7. The significance of this is that it suggests that the simpler model would lead to early separation. With the full Reynolds stress model one sees that the displacement thickness is in excellent agreement with the data (figure 5). The skin friction is only a bit low at the last measurement point.

The two mean velocity profiles provided by figure 8 of Samuel & Joubert (1974) were

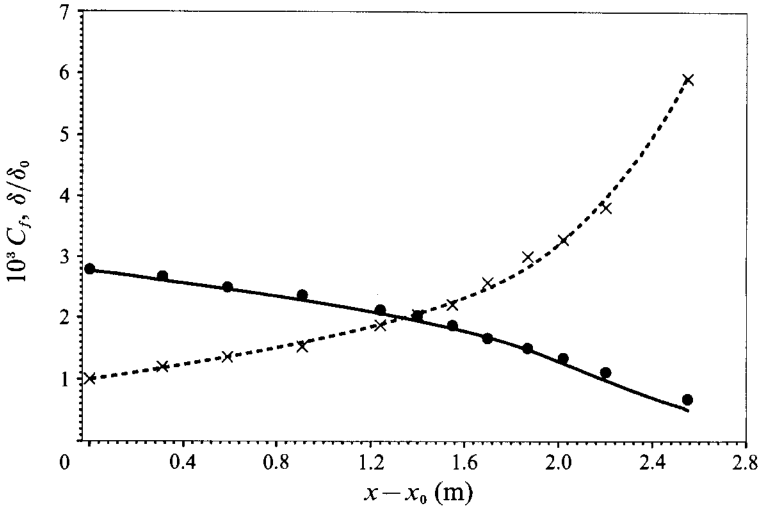

FIGURE 5. Friction coefficient (●) and displacement thickness (×) versus downstream distance for the Samuel & Joubert experiment.

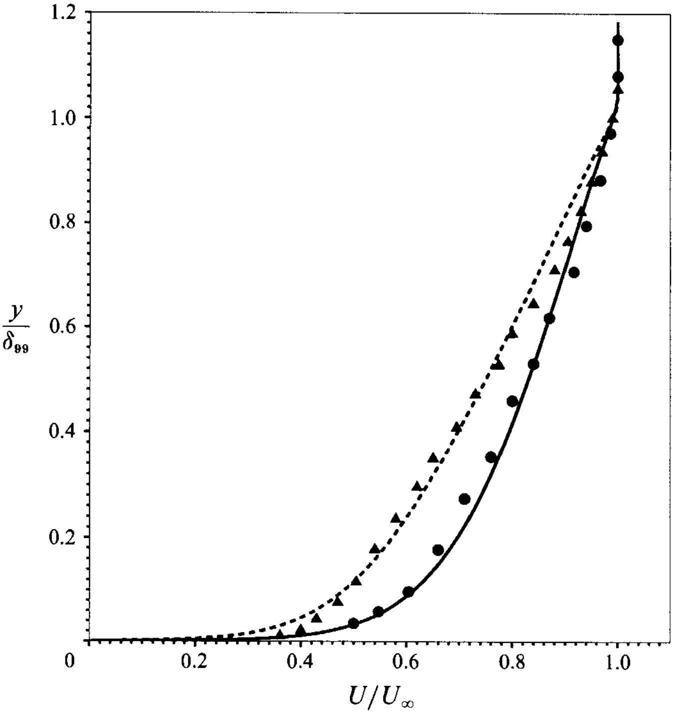

FIGURE 6. Mean velocity profiles at stations 9 (●) and 12 (△) of the Samuel & Joubert adverse-pressure-gradient boundary layer. Model predictions: ——, station 9; - - -, station 12.

transcribed, and are shown here, along with model predictions, in figure 6. Station 9 is at $x - x_0 = 1.87$ m, and is well into the adverse-pressure-gradient region. Station 12 is the last measurement point, at $x - x_0 = 2.55$ m. The model predicts the evolution of the mean flow reasonably well, although the shear is a bit low near the surface at station 12. The central portion of the profiles shows the characteristic adverse-pressure-gradient form, with a large wake defect and a nearly linear shear.

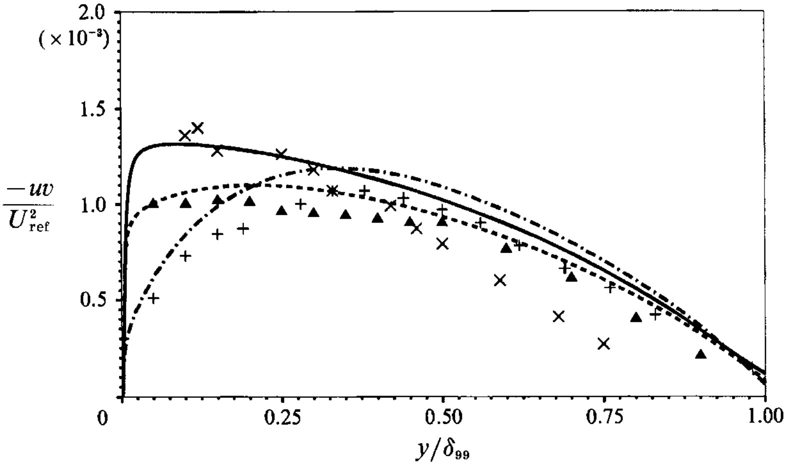

FIGURE 7. Reynolds shear stress profiles at stations T1 (×, ——), T4 (▲, - - - -) and T6 (+, –·–·–) of Samuel & Joubert.

Reynolds shear stress profiles were transcribed from figure 13 of Samuel & Joubert and are presented along with model results in figure 7. The measurement stations are: T1, $x-x_0 = 0.19$ m; T4, $x-x_0 = 1.53$ m; T6, $x-x_0 = 2.54$ m. The qualitative evolution of the profiles in the region near the wall is reproduced well by the model. The tendency for the maximum stress to move to the middle of the layer by station T6 is also reproduced. The most glaring discrepancy between model and data occurs in the outer half of the boundary layer at station T1. Here the model is well above the data. At station T1 the pressure gradient has had a small effect on the boundary layer, which is still similar to a zero-pressure-gradient layer. Indeed the over prediction of $-\overline{uv}$ here is similar to that shown by figure 4 for the outer region of the zero-pressure-gradient layer. This would seem to be one of the many difficulties that closure models have with the outer part of boundary layers. That part of the layer is the intermittent region, in which irrotational fluctuations play a significant role. Fortunately, it is also a region of small mean shear, so most transport properties of the boundary layer can be predicted reasonably well despite the poor representation of the outermost regions.

The 'universal' law of the wall is a constant-stress layer, with logarithmic mean velocity and constant Reynolds stresses. This is the form invoked in the wall-function method. Figure 7 shows clearly that the near-wall region of adverse-pressure-gradient boundary layers can depart substantially from a constant-stress layer. In fact, the profile at T6 has nearly a linear stress layer. It is rather gratifying that the present model can compute this type of non-universal wall layer.

The results for the Samuel & Joubert boundary layer indicate that the full Reynolds stress model may have significant advantages in a boundary layer subject to a large pressure rise. The Schubauer & Spangenberg (1960) experiment provides data for such a case. These data are tabulated in Coles & Hirst (1968). In the experiment, a boundary layer developed in zero pressure gradient to an R_m of 4016, at which point an adverse pressure gradient was applied. The flow developed downstream past separation. The last measurement point was just upstream of the region where dust released at the surface showed evidence of backflow. Figures 8 and 9 show friction coefficient and displacement thickness for the Schubauer & Spangenberg experiment B. The friction coefficient in the figures is based on the local free-stream velocity, while δ_* is again normalized by its initial value.

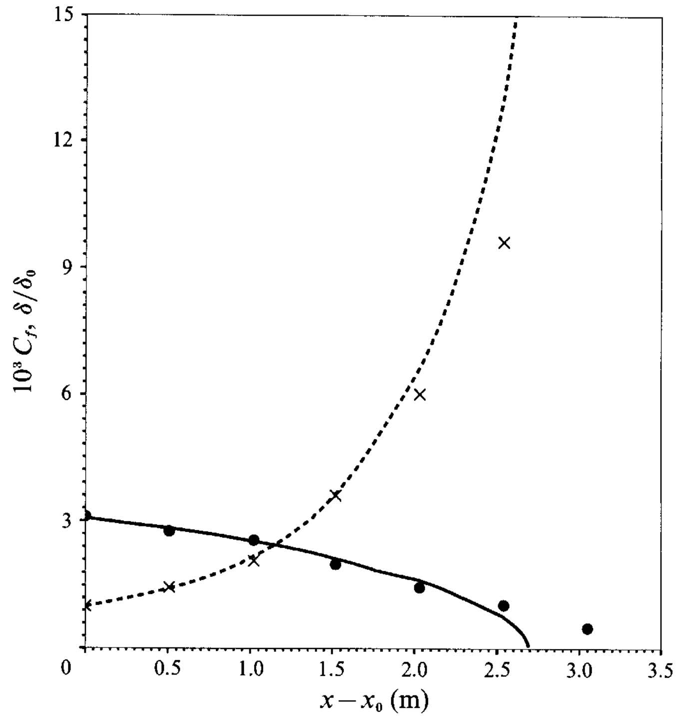

FIGURE 8. Friction coefficient (●) and displacement thickness (×) from Schubauer & Spangenberg. The predictions are by the simplified k–ϵ–$\overline{v^2}$ version. Premature separation is indicated at $x - x_0 = 2.7$.

In figure 8 the data are compared to the k–ϵ–$\overline{v^2}$ version of the model. In that version only the k–ϵ and $\overline{v^2}$–$\not{h}_{22}$ systems of equations are solved, while $-\overline{uv}$ is modelled by the eddy viscosity formula $C_\mu \overline{v^2} T \partial_y U$, with T as in (6). Figure 8 shows more obviously the failure of the eddy-viscosity approximation that was beginning to emerge at the last measurement point of the Samuel & Joubert experiment: the displacement thickness is growing too rapidly, and separation occurs prematurely. In this case, the boundary-layer code blew up at an $x - x_0$ of about 2.7 m, where the friction velocity seemed to go to zero. In the experiments back flow was observed downstream of 3 m. We expected that the early separation was in large part due to the use by the k–ϵ–$\overline{v^2}$ version of an eddy viscosity in the mean momentum equation. The eddy-viscosity approximation corresponds to an equilibrium assumption for the Reynolds shear stress; such an assumption fails when the upstream history of stress evolution strongly affects its downstream behaviour. This rationalization for the failure of the mean momentum eddy viscosity was one motivation for exploring the full Reynolds stress version of our model.

The full Reynolds stress version did not have the difficulty of the simpler eddy viscosity version. In figure 9 it is shown how this model does a better job of predicting the variation of displacement thickness and skin friction. The friction coefficient still drops below the data, but it does not go to zero. At the last measurement point the experimental friction coefficient is somewhat questionable: it was inferred by Schubauer & Spangenberg (1960) from a Clauser plot, which relies on a well-developed logarithmic region. In fact the mean flow profile at that location seemed to have a limited contact with the logarithmic line, and such contact would be forced by the

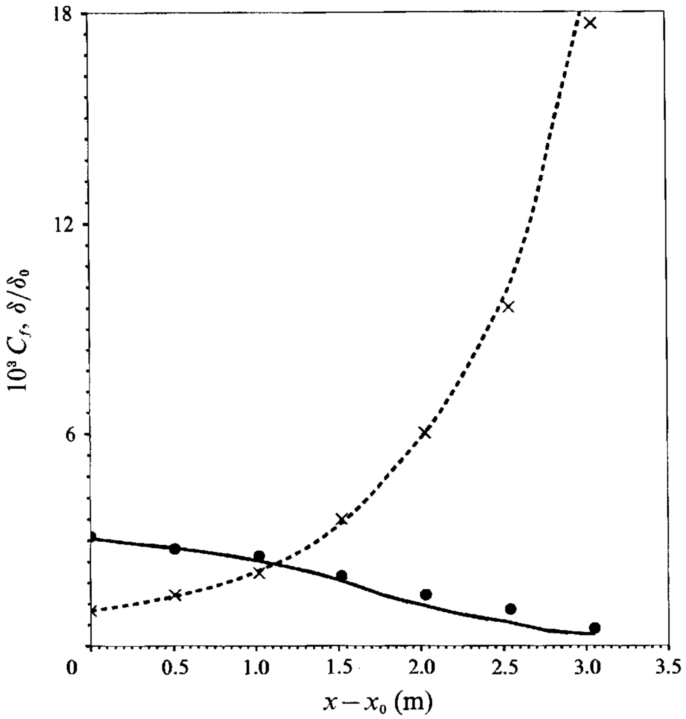

FIGURE 9. The same data as in figure 8 are compared to the full Reynolds stress version of the model. The behaviour in the region of small skin friction is predicted more accurately than by the simplified version.

method of determining u_*. Schubauer & Spangenberg expressed some consternation that their C_f was not heading towards zero as the separation was approached; this could have been due to their use of the Clauser plot.

Figure 10 shows comparisons of mean velocity profiles to measurements at various downstream positions. The agreement is reasonable, although the location farthest downstream shows significant discrepancies near the top of the boundary layer. Broadly speaking, the transition from a zero pressure gradient to an adverse pressure gradient form of mean flow profile is described correctly by the model.

The solution for the Reynolds stress components showed how they respond to an applied adverse pressure gradient. Figure 11 shows the model's prediction for the evolution of the kinetic energy profile with downstream distance in the Schubauer & Spangenberg experiment. Qualitatively, this is similar to the evolution observed by Samuel & Joubert (1974): the near-wall peak in the upstream profiles is reduced in magnitude, and moved toward the wall by the adverse pressure gradient; downstream the near-surface peak has been suppressed and the maximum kinetic energy occurs in the middle of the boundary layer. The shapes of the downstream profiles as a function of y/δ_{99} are far from those of a zero-pressure-gradient boundary layer. These distributions of turbulent intensity determine transport properties and the evolution of the flow: for this reason, we suspect that a second-order closure must have the flexibility to predict these dramatic changes of the turbulence statistics if it is to cope with non-equilibrium flow. Indeed, the primary motivation for developing a near-wall model, rather than simply prescribing universal wall functions, is the desire to compute flows in which the wall region is not universal.

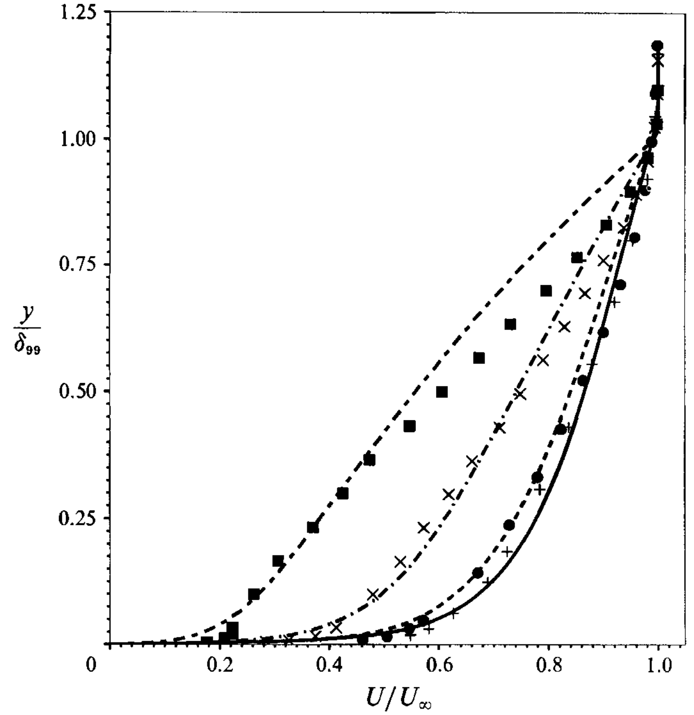

FIGURE 10. Mean velocity profiles computed by the full Reynolds stress model for the Schubauer & Spangenberg flow. Downstream positions: +, ——, $x = 0$; ●, – – – 1.016 m; ×, —·— 2.032 m; ■, ——— 3.048 m.

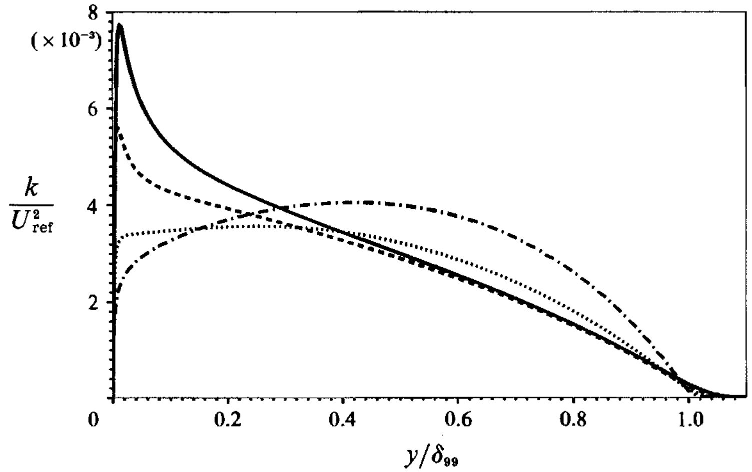

FIGURE 11. Profiles of turbulent kinetic energy at $x = 0$ (solid), 1.016 m (dashed), 2.032 m (dotted) and 3.048 m (dash-dot) in the Schubauer & Spangenberg boundary layer, as computed by the present model.

5. The boundary layer on a convexly curved surface

The present model is coordinate-system independent. This means that the empirical constants can be obtained from data on a simple flow, in the present case two-dimensional plane channel flow, while the model can be used in a wide range of flows.

For non-planar cases, curvilinear coordinates can be adopted. In this section results for a boundary layer on a convexly curved wall are presented.

The governing equations (1), (8), (12), (13) and the mean momentum and continuity equations can be transformed to curvilinear coordinates by techniques of classical differential geometry (McConnell 1957), as discussed in Appendix B. The equations are used in their two-dimensional boundary-layer approximation. Additionally, some $O(\delta/R_c)$ terms will be dropped from the turbulent transport of Reynolds stress. These terms are described in Appendix B: formally they can be omitted in the limit $\delta/R_c \ll 1$ with $\delta U_\infty/R_c u_*$ of $O(1)$. Computations were done with these terms included and found numerically to be extremely close to other computations in which they were omitted. Their omission simplifies the presentation of equations. With this simplification, the curvature terms assume a rather obvious form. The equations are in local plane polar coordinates: $\mathrm{d}y$ is the radial direction, normal to the wall, with $y=0$ at the wall; $\mathrm{d}\phi$ is the tangential direction, but we will adopt the usual surface coordinate $\mathrm{d}x = R_c\,\mathrm{d}\phi$ (Johnston 1978). With these definitions, terms which would be $1/r\,\partial_\phi$ in polar coordinates become $1/\alpha\,\partial_x$ in the present equations, where $\alpha \equiv 1+y/R_c$.

5.1. *Mean flow*

With the boundary-layer approximation the equations of the mean flow are

$$\left.\begin{aligned}\frac{U}{\alpha}\partial_x U + V\partial_y U + \frac{UV}{\alpha R_c} &= -\frac{1}{\alpha}\partial_x \mathscr{P} + \nu\,\partial_y^2 U - \partial_y \overline{uv} - 2\frac{\overline{uv}}{\alpha R_c},\\ \frac{U^2}{\alpha R_c} + \frac{\overline{u^2}-\overline{v^2}}{\alpha R_c} &= \partial_y(\mathscr{P}+\overline{v^2}),\\ \partial_x U + \partial_y(\alpha V) &= 0,\end{aligned}\right\} \tag{19}$$

where U is the ϕ-component of velocity and V is the r-component, in polar coordinates. A term $\nu(U/\alpha R_c - \partial_y U)/\alpha R_c$ was dropped from the U-equation because viscous terms are significant only in a wall layer, in which curvature is insignificant. $\overline{v^2}$ can be absorbed into the definition of $\mathscr{P}$ since the extra term which this produces in the x-momentum equation is negligible in the boundary-layer approximation; hence $\overline{v^2}$ can be eliminated from the right-hand side of the y-momentum equation by redefining $\mathscr{P}$. Also, the turbulent term on the left-hand side of this equation is small compared to the mean flow term and will be dropped.

Continuity is satisfied by introducing a stream function, such that

$$U = \partial_y \Psi; \quad \alpha V = -\partial_x \Psi. \tag{20}$$

If the independent variables in (19) are changed from x and y to x and Ψ then the simpler form

$$\left.\begin{aligned}U\partial_x U &= -\partial_x \mathscr{P} + \nu\,\partial_y^2 U - \partial_y(\alpha\overline{uv}) - \overline{uv}/R_c,\\ U^2/\alpha R_c &= \partial_y \mathscr{P}\end{aligned}\right\} \tag{21}$$

emerges. Note that this is just a change of variables; the velocity components are still referred to plane polar coordinates. The x-derivatives in (21) are at constant Ψ, and ∂_y is understood to mean $U\partial_\Psi$. Equations (21) were used for numerical computations. In those computations an expanding grid was introduced by further changing the independent variable to $\eta = \Psi/\Psi_{99}$ where Ψ_{99} is a function of x defined as the location where $U = 0.99U_\infty$. Ψ_{99} was found by solving the equation $U(\eta=1) = 0.99U_\infty$ in conjunction with (21). The boundary conditions are $U=0$ at $y=0$ and $\partial_\Psi U \rightarrow -1/\alpha R_c$ as $y \rightarrow \infty$. The latter condition is compatible with (21) in the free stream, where viscous and Reynolds stresses are negligible.

5.2. *Reynolds stress model*

In polar coordinates, with the independent variables changed to Ψ and x, the equations (1) for the Reynolds stresses transform to

$$\left.\begin{aligned}
\frac{U}{\alpha}\partial_x \overline{u^2}+2\frac{U}{R_c\,\alpha}\overline{uv} &= P_{11}+\not{p}_{11}-\frac{\epsilon}{k}\overline{u^2}+\nu\,\partial_y^2\,\overline{u^2}+\frac{1}{\alpha}\partial_y\left(\alpha\frac{\nu_{\mathrm{T}_{22}}}{\sigma_k}\partial_y\,\overline{u^2}\right),\\
\frac{U}{\alpha}\partial_x \overline{v^2}-2\frac{U}{R_c\,\alpha}\overline{uv} &= P_{22}+\not{p}_{22}-\frac{\epsilon}{k}\overline{v^2}+\nu\,\partial_y^2\,\overline{v^2}+\frac{1}{\alpha}\partial_y\left(\alpha\frac{\nu_{\mathrm{T}_{22}}}{\sigma_k}\partial_y\,\overline{v^2}\right),\\
\frac{U}{\alpha}\partial_x \overline{uv}+\frac{U}{R_c\,\alpha}(\overline{v^2}-\overline{u^2}) &= P_{12}+\not{p}_{12}-\frac{\epsilon}{k}\overline{uv}+\nu\,\partial_y^2\,\overline{uv}+\frac{1}{\alpha}\partial_y\left(\alpha\frac{\nu_{\mathrm{T}_{22}}}{\sigma_k}\partial_y\,\overline{uv}\right).
\end{aligned}\right\}\qquad (22)$$

Some terms that are $O(\delta/R_c)$ smaller than those included in (22) have been dropped from the turbulent transport model – as discussed in Appendix B. They were indeed found to be numerically small.

The components of the Reynolds stress production tensor are

$$P_{11}=-2\overline{uv}\,\partial_y\,U,\quad P_{22}=2\overline{uv}\frac{U}{\alpha R_c},\quad P_{12}=-\overline{v^2}\,\partial_y\,U+\overline{u^2}\frac{U}{\alpha R_c}.\qquad (23)$$

$P=-\overline{uv}\,\partial_y\,U+\overline{uv}U/\alpha R_c$ is the rate of turbulent kinetic energy production, equal to one-half the trace of P_{ij}. The elliptic model (8) for $\not{p}_{ij}$ becomes

$$L^2\left(\frac{1}{\alpha}\partial_y(\alpha\,\partial_y f_{ij})-\frac{2}{\alpha^2R_c^2}f_{ij}+2\gamma^i_{1k}\,\gamma^j_{11}f_{kl}\right)-f_{ij}=-\Pi_{ij},\qquad (24)$$

and $\not{p}_{ij}=kf_{ij}$. The left-hand side is the elliptic relaxation operator $L^2\nabla^2 f_{ij}-f_{ij}$, expressed in polar coordinates, with x-derivatives neglected by the boundary-layer approximation. γ^i_{jk} is defined in Appendix B: its only non-zero components are $\gamma^1_{12}=-\gamma^2_{11}=1/\alpha R_c$. Actually, the last two terms inside the big parenthesis are of relative order $(\delta/R_c)^2$ and can safely be omitted. The k–ϵ system is essentially as in (12) and (13), with the turbulent transport terms replaced by $1/\alpha\,\partial_y(\alpha\,...)$, as in (22).

5.3. *Results*

The baseline experiment in Gillis *et al.* (1980) and Simon *et al.* (1982) is a boundary layer in zero pressure gradient throughout, which develops on an upstream flat plate to a momentum-thickness Reynolds number $R_m=4200$; it then enters a 90° constant-curvature bend, from which it exits into another flat-plate section. At the start of curvature the ratio of boundary-layer thickness to surface radius of curvature is $\delta/R_c=0.1$. In order to maintain zero surface pressure gradient on the curved section the wall opposite to the test surface was flared out near the start of curvature and flared in near its end. The care taken to isolate convex curvature from pressure gradient effects distinguishes these experiments from others in the field.

The present numerical computations are of the Gillis & Simon baseline experiments. A flat-plate boundary layer was computed by initializing the profiles with Spalart's (1988) DNS data at $R_m=670$, then integrating the model downstream to $R_m=4200$. It was shown in figure 3 that the model gives a good representation of the Reynolds-number dependence of zero-pressure-gradient flat-plate boundary layers, so this is a satisfactory initialization procedure. Curvature was then introduced abruptly by setting $R_c=10\delta$. Although this causes a discontinuity, its effect dies away very quickly.

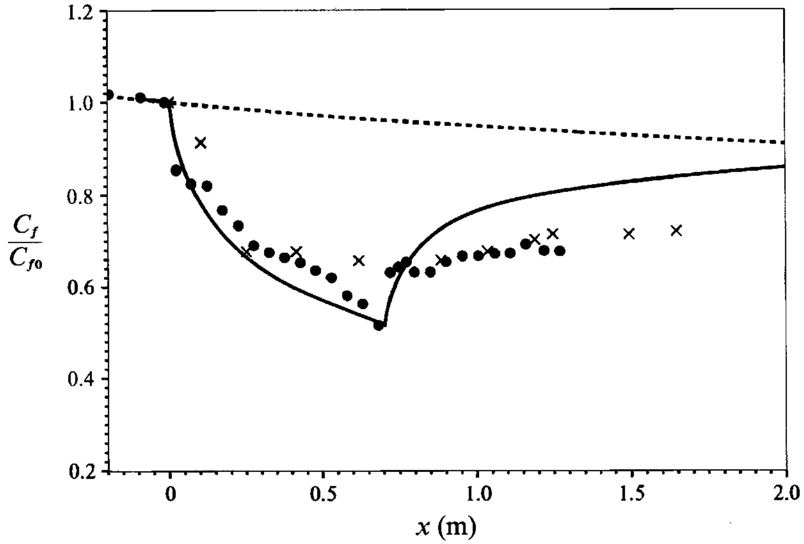

FIGURE 12. Solid line is computed skin friction, normalized on its value at the start of curvature; dashed line is normalized skin friction computed for a flat-plate boundary layer. Experimental data on skin friction (×) from Gillis *et al.* and surface heat flux (●) from Simon *et al.*

A computation was done in which curvature was introduced more gradually and the results were found to be essentially the same as for the abrupt case. In the experiments the 90° bend was 0.7 m long and the unit Reynolds number was $9.87 \times 10^5\ \mathrm{m}^{-1}$. This unit Reynolds number was used to convert the numerical downstream coordinate to metres. The curvature was set to zero at $x = 0.7$ m in the numerical solution and the computation continued into the downstream recovery region.

Figure 12 shows the skin friction, normalized on its value at the start of curvature. Experimental data on skin friction from Gillis *et al.* (1980) and surface heat flux from Simon *et al.* (1982) are included in the figure; both are normalized by their value at the start of curvature. The weak Reynolds' analogy is that skin-friction and heat-transfer coefficients are proportional to one another: on the basis of this analogy, the above normalization should make the skin-friction and heat-flux data comparable. The motive for including the heat-transfer data is that it was measured directly, while the skin friction was only inferred by fitting measured mean velocity profiles to a universal log-law. In the curved section there is no constant-stress layer, and hence no theoretical basis for assuming the universal log-law to exist. The agreement between the data sets in figure 1 suggests that the skin-friction measurements are largely reliable. However, Bandyopadhyay & Ahmed (1993) found unambiguous departure from the universal low-law in a curved-wall boundary layer ($0.04 < \delta/R_c < 0.14$), and that log-law estimates of skin friction were erroneous.

The dashed line in figure 12 is the normalized skin friction computed for a flat-plate boundary layer; the solid line is the solution for the curved wall. Both the model and data show an abrupt drop in skin friction at the onset of curvature. By the end of the curved section, at $x = 0.7$ m, the skin friction is nearly one half its level at the start of curvature ($x = 0$). After the curved section the skin friction recovers toward its flat-plate level. Both the Simon *et al.* data and the model show an immediate, abrupt response at the end of curvature, but the model solution continues to rise, asymptoting toward the dashed line. The experimental data level out after the initial rise and show little tendency to approach the unperturbed flat-plate level. It was noted by Gillis that

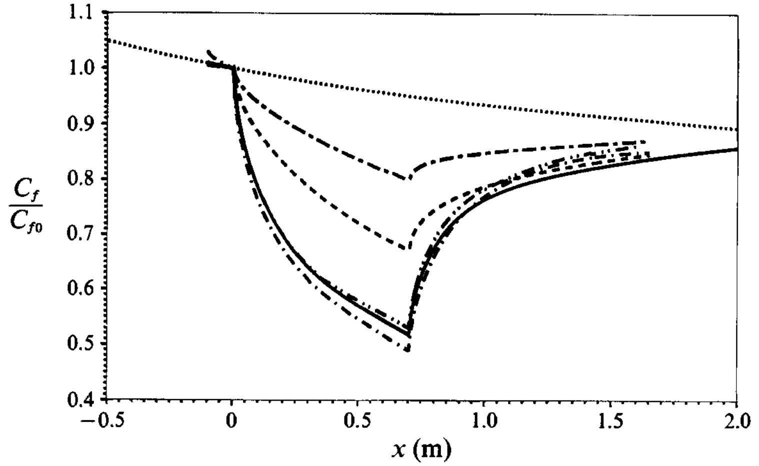

FIGURE 13. Dependence of skin friction versus x on curvature and Reynolds number. —·—, $R_m = 1900$, $\delta/R_c = 0.05$. $R_m = 4200$: ———, $\delta/R_c = 0.025$; ---, $\delta/R_c = 0.05$; ——, $\delta/R_c = 0.1$. —··—, $R_m = 8400$, $\delta/R_c = 0.2$. ..., flat wall.

a secondary flow was present downstream of the curve, despite significant efforts to eliminate it; it is possible that this secondary flow slows the recovery process. The experiment of Alving, Smits & Watmuff (1990) showed a clear recovery to equilibrium following a curved section. Their experiment was at a higher Reynolds number and contained significant streamwise pressure gradients.

The fact that the model recovers toward the flat-plate solution is inevitable: the present type of turbulence model is formulated to produce parabolic relaxation with downstream distance toward an equilibrium flow. Despite the quantitative discrepancies in the recovery region, it is significant that the model reproduces the prompt response at the onset of curvature and the far more gradual recovery downstream. The experimenters attributed the slow recovery to a reorganization by curvature of the turbulent eddy structure. However, the present single-point Reynolds stress model contains no obvious representation of eddy structure, yet it produces the same asymmetric response observed experimentally. It would seem that the timescale that enters the parabolic, eddy diffusive, relaxation process controls the rate of recovery, while the timescales associated with mean shear and curvature control the initial response. The asymmetry in the model response then would reflect the disparity between inertial and (eddy) viscous timescales, rather than structural reorganization *per se*. A corollary to these remarks is that overprediction of the rate of recovery from curvature is due to inadequacies in the gradient transport model for turbulent self-diffusion.

Simon *et al.* (1982) also measured the Stanton number ($St \equiv Q_{\text{wall}}/\rho C_p U_\infty(T_{\text{wall}} - T_\infty)$) in a boundary layer with $\delta/R_c = 0.05$. They found that the Stanton number versus x curve was changed very little from that displayed by figure 12. From this they concluded that strong curvature organizes the boundary layer such that it becomes insensitive to the precise level of curvature. However, a caveat must be made about that conclusion: to produce a lower value of δ/R_c in the apparatus used by Simon *et al.* it was necessary to lower the Reynolds number at the start of the curved section; the $\delta/R_c = 0.05$ case had $R_m = 1900$. Figure 13 shows model C_f computations at $R_m = 1900$ with $\delta/R_c = 0.05$ at the start of curvature, along with solutions at $R_m = 4200$ and $\delta/R_c = 0.1$. The model solution concurs with Simon *et al.*'s finding that these two cases have nearly equal St versus x profiles. The figure also contains solutions

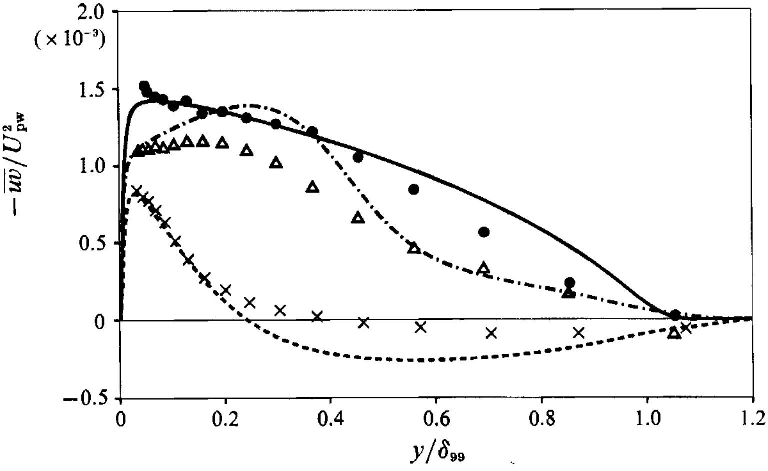

FIGURE 14. Model solutions and experimental data on $-\overline{uv}/U_{pw}^2$. The profiles are at $x = -0.062$ m (●, ——), $x = 0.162$ m (×, – – –) and $x = 1.124$ m (△, —·—·—). These stations are upstream of the bend, 20.6° around the bend and in the downstream recovery region.

at $R_m = 4200$ with $\delta/R_c = 0.05$ and 0.025, and at $R_m = 8400$ with $\delta/R_c = 0.2$. Clearly, at fixed Reynolds number the Stanton number is sensitive to the level of curvature, contrary to Simon *et al.*'s inference. The present results do not support the conclusion that curvature organizes the boundary-layer turbulence so that C_f becomes insensitive to δ/R_c. Bandyopadhyay & Ahmed (1993) proposed that the Reynolds number based on radius of curvature ($u_* R_c/\nu$) was a controlling parameter. The cases of $R_m = 1900$, $\delta/R_c = 0.05$, $R_m = 4200$, $\delta/R_c = 0.1$ and $R_m = 8400$, $\delta/R_c = 0.2$ have similar curvature Reynolds numbers, so the agreement between the C_f curves of these cases is consistent with the proposal by Bandyopadhyay & Ahmed.

When the skin friction drops, less mean momentum is being transported from the free stream to the surface. Immediately next to the surface the transport is accomplished by molecular viscosity, but in the bulk of the boundary layer it is carried by the Reynolds shear stress. Hence, the reduction in skin friction should have its counterpart in a reduced Reynolds shear stress. Figure 14 contains model solutions and experimental data on $-\overline{uv}$. They are normalized by $U_{pw} = \lim_{y\to\infty}(\alpha U)$; this velocity is the extrapolation of the potential flow outside the boundary layer to the wall (Gillis *et al.* 1980). U_{pw} is constant around the bend (15 m/s in the baseline experiments). The profiles in figure 14 are at $x = -0.062$ m, 0.162 m and 1.124 m. These stations are upstream of the bend, 20.6° around the bend and in the downstream recovery region. The profile within the curved section shows how curvature suppresses Reynolds stress in the outer region to the extent that it drives $-\overline{uv}$ negative; the mean shear is positive throughout the boundary layer, so the region of negative $-\overline{uv}$ could be described as a region of 'counter-gradient' transport. Of course, the gradient transport approximation was not used in the mean momentum equation; indeed, the failure of gradient transport in strongly curved flow provides one of many motivations for the present Reynolds stress modelling. The suppression of Reynolds shear stress by curvature was first measured by So & Mellor (1973). Like Gillis *et al.* they concluded that the stress in the outer part of the boundary layer was quenched by the centrifugal stabilization.

The profile in figure 14 downstream of the bend (dash-dot line) shows how the stress recovers first near the wall and then this recovery propagates out across the boundary

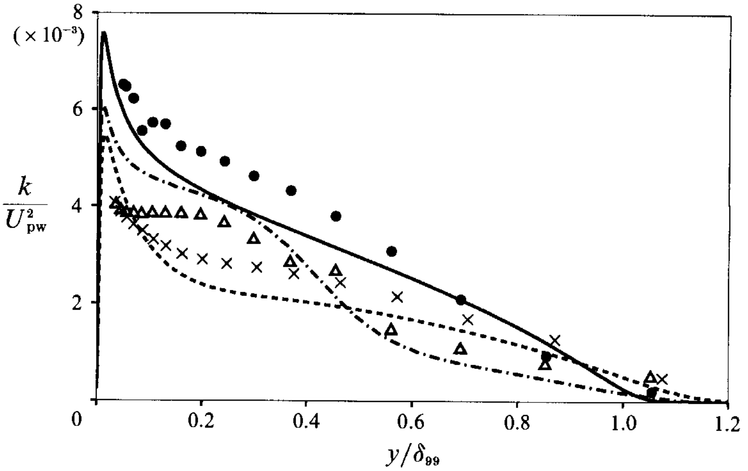

FIGURE 15. The kinetic energy, at the same locations as in figure 14.

layer; Alving *et al.* (1990) referred to this as a 'stress bore'. The model shows more rapid recovery than the experimental data, as was already seen in figure 1; however, the qualitative features of the model solution are remarkably similar to those of the data.

In the neighbourhood of the wall the profile at $x = 0.162$ m, within the bend, is in good agreement with data, but in the outer region the tendency for $-\overline{uv}$ to go negative is exaggerated by the model. The negative shear stress causes negative energy production in this region and this reduces the turbulent kinetic energy. The kinetic energy, at the same locations as in figure 14, is plotted in figure 15. The kinetic energy drops below the data in the curved section, consistently with the excessive negative production, but shows the same qualitative features as the data. Recovery again is in the form of a 'bore' propagating away from the wall. The tendency for the energy profile to develop a flat plateau, which is shown in Gillis' data, and was noted by him, is less pronounced in the model solution.

The origin of the negative Reynolds shear stress was investigated by plotting the $-\overline{uv}$ budget. In the flat, upstream section the balance in the outer part of the layer is predominantly between shear production and redistribution; the redistribution is negative everywhere in that region and nearly equal and opposite to shear production. A stress budget just after the start of the curved section is contained in figure 16. Shear production $(\overline{v^2}\,\partial_y U)$ is the chain-dot curve and the chain dash curve is the sum of the redistribution term $(-\wp_{12})$ and $\overline{uv}/T$: this can be regarded as the sum of redistribution and anisotropic dissipation. The peaks of these curves overflow the plotting limit, showing that in the neighbourhood of these peaks the dominant balance is still between shear production and redistribution. The curvature production $(-\overline{u^2}U/R_c\,\alpha$; dashed line) is significant near the wall, but it becomes predominant in the outer portion of the boundary layer. It counteracts the shear production, thereby suppressing $-\overline{uv}$: the solid line is $D_t(-\overline{uv})$ and shows that $-\overline{uv}$ is decreasing with downstream distance. (NB, the signs in figure 16 are such that the segmented curves sum to the solid curve.) The suppression of $-\overline{uv}$ in the outer region occurs because the shear production falls off more rapidly with increasing y than the (negative) curvature production; the latter thereby becomes dominant when $y > 0.3\delta_{99}$. It is curious that the redistribution actually becomes slightly positive in the outermost part of the layer and assists shear production in balancing the negative curvature production. Transport (dotted line),

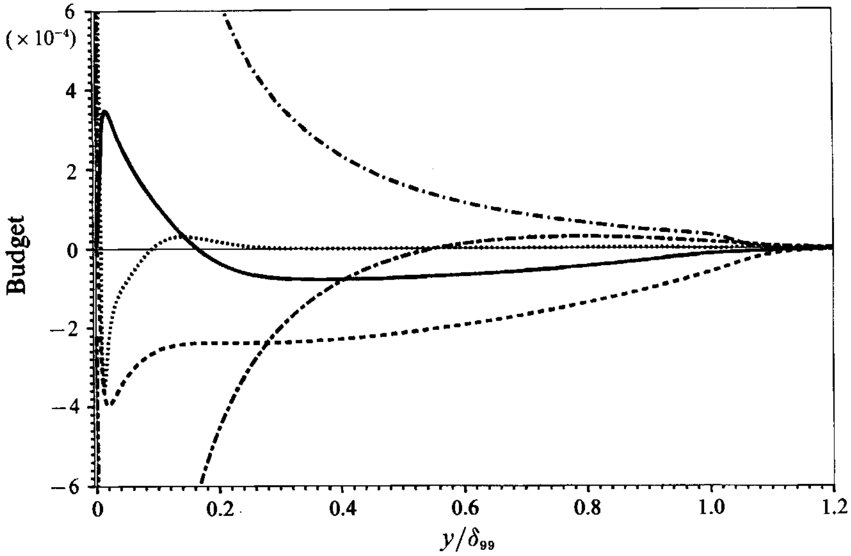

FIGURE 16. Reynolds shear stress budget just after the start of the curved section. Shear production ($v^2\partial_y U$), —·—; redistribution plus dissipation ($\wp_{12}+\overline{uv}/T$), ———; production by curvature ($-u^2U/R_c\alpha$), ---; $D_t(-\overline{uv})$, ——; sum of molecular and turbulent transport, ...

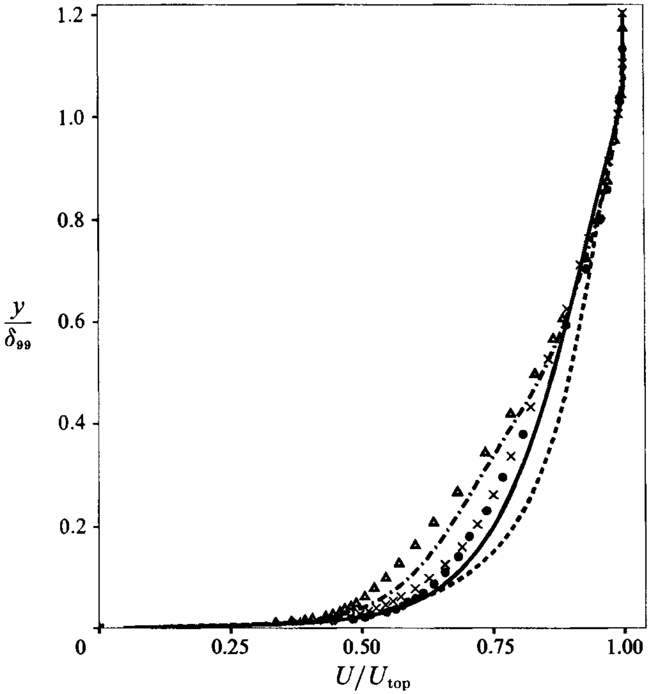

FIGURE 17. Mean velocity profiles upstream, in a bend and downstream. $x = -0.413$ m (●; ——); $x = 0.162$ m (×; ---); $x = 1.124$ m (△; —·—). See figures 14 and 15.

which is a combination of molecular and turbulent contributions, is significant only near the wall.

Mean velocity profiles are shown in figure 17. The upstream profile is at $x = -0.413$ m, rather than the location of figures 14 and 15, because this was the last station upstream of curvature at which the mean flow was measured. The other locations are the same as in figures 14 and 15. The velocity is normalized by its level at the top of the boundary layer, which is the free-stream velocity in the flat sections. The model is showing an alteration of the profile within the curved section, while the data show the profile there to have the same form as upstream. It is not clear why the data show no effect of curvature on the velocity profile. In the downstream recovery region the mean flow profile is less full than an equilibrium flat-plate profile. This feature is present in both model and data, but again the model is showing a more rapid recovery toward equilibrium.

6. Heat flux modelling

The curved-wall boundary layer is a useful flow in which to consider heat flux modelling. The $\overline{u\theta}$- and $\overline{v\theta}$-components are intimately coupled by the curvature. In a flat-plate boundary layer $\overline{u\theta}$ is much bigger than $\overline{v\theta}$, but it plays no role in the mean heat transfer from a uniformly heated surface.

The mean temperature is the solution to

$$U\partial_x\Theta+V\partial_y\Theta=-\partial_i\overline{u_i\theta}+\kappa\nabla^2\Theta. \tag{25}$$

The exact heat-flux equation in Cartesian coordinates is

$$U\partial_x\overline{u_i\theta}+V\partial_y\overline{u_i\theta}=-\overline{u_iu_j}\,\partial_j\Theta-\overline{u_j\theta}\,\partial_j U_i+\wp_{\theta_i}+\tfrac{1}{2}(\kappa+\nu)\nabla^2\overline{u_i\theta}-\partial_j\overline{u_ju_i\theta}, \tag{26}$$

where $-\overline{u_j\theta}\,\partial_j U_i$ is the production from mean shear and $-\overline{u_iu_j}\,\partial_j\Theta$ is the production from mean temperature gradient.

$$\wp_{\theta_j}=-(1/\rho)\overline{\theta\partial_i p}-(\kappa+\nu)\overline{\partial_j u_i\partial_j\theta}+\tfrac{1}{2}(\kappa-\nu)\,\partial_j(\overline{u_i\partial_j\theta-\theta\partial_j u_i}) \tag{27}$$

is analogous to the redistribution term in the Reynolds stress transport equations (1). Of course the trace of $\wp_{\theta_i}$ is not zero, and here the term should not be understood to redistribute heat flux.

The elliptic relaxation model (8) was devised primarily to represent kinematic blocking by boundaries (Durbin 1991). Its most pronounced effect is to suppress $\overline{v^2}$ near the surface. The effect on the mean momentum flux, $-\overline{uv}$, is much smaller; indeed it is shown in Durbin (1991, 1992) that an equilibrium, eddy-viscosity model will often be satisfactory for $-\overline{uv}$, provided that the eddy viscosity is formed from $\overline{v^2}$ and that kinematic blocking is accounted for in the $\overline{v^2}$-model. One expects that similar considerations apply to the heat flux: once the kinematic blocking of $\overline{v^2}$ has been included, the heat flux model can be of the usual quasi-homogeneous type. Actually, some calculations were done with an elliptic model for $\wp_{\theta_i}$, but the results were very little different form the simpler model to be described. The principal drawback to the quasi-homogeneous formulation is that it precludes satisfaction of the correct boundary conditions on $\overline{u_i\theta}$ at the wall.

The last term of (26) represents turbulent transport. We adopt the usual gradient transport model:

$$-\partial_j\overline{u_ju_i\theta}=\partial_j\frac{\nu_{\mathrm{T}_{jk}}}{\sigma_\theta}\partial_k\overline{u_i\theta}. \tag{28}$$

Following Launder (1989), $\sigma_\theta=1.5$.

The technique of invariant closure modelling could be used to write the most general closure for $\wp_{\theta_i}$. This was done by Dakos & Gibson (1987) and need not be repeated here. In fact, we will simply adopt an analogy to (11) for our heat-flux model: $\wp_{\theta_i}$ is

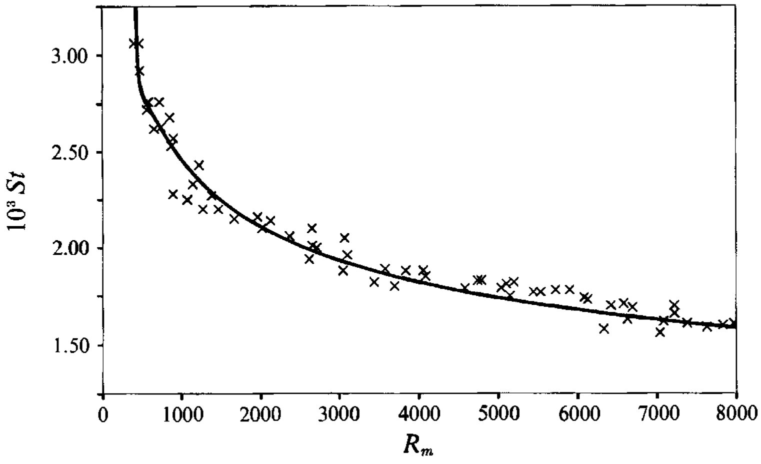

FIGURE 18. Stanton number *vs.* momentum-thickness Reynolds number in a zero-pressure-gradient boundary layer. Data from Reynolds *et al.* (1958).

written as the sum of a return to isotropy term and 'isotropization' of production terms,

$$\wp_{\theta_i} = -(C_{\theta_1}\epsilon/k)\overline{u_i\theta} + C_{\theta_2}\overline{u_iu_j}\,\partial_j\Theta + C_{\theta_3}\overline{u_j\theta}\,\partial_j U_i. \tag{29}$$

The constants of the model (29) were determined by the following considerations.

(i) By dropping the transport terms from (26), in a flat-plate boundary layer one obtains the eddy diffusion formula

$$-\overline{v\theta} = \frac{1-C_{\theta_2}}{C_{\theta_1}}\overline{v^2}T\partial_y\Theta,$$

where $T = k/\epsilon$. This is the k–ϵ–$\overline{v^2}$ model (Durbin 1991). Comparing this to $\nu_{T_{22}}$ in (5), one finds the turbulent Prandtl number $(\nu_\mathrm{T}/\kappa_\mathrm{T})$ to be

$$Pr_\mathrm{T} = C_\mu C_{\theta_1}/(1-C_{\theta_2}). \tag{30}$$

The present value of C_μ is 0.23 and for turbulent boundary layers in air $Pr_\mathrm{T} \approx 1$. Hence (30) imposes the condition that $C_{\theta_1}/(1-C_{\theta_2}) \approx 4$; computations of flat-plate boundary-layer heat transfer are relatively insensitive to the precise values of C_{θ_1} and C_{θ_2} as long as this ratio is near 4. Figure 18 shows a computation of Stanton number versus momentum-thickness Reynolds number in a zero-pressure-gradient boundary layer with the present values of $C_{\theta_1} = 2.5$ and $C_{\theta_2} = 0.45$. The agreement with the data from Reynolds, Kays & Kline (1958) is quite good.

(ii) In principle data on $\overline{u\theta}$ in flat-plate boundary layers could be used to determine C_{θ_3}. In practice those data are somewhat unreliable, but can be used as a rough guide. In figure 19 the data of Subramanian & Antonia (1981) are shown along with model solutions with $C_{\theta_3} = 0$. The data band is not due to experimental scatter, but represents the range of measured $\overline{u\theta}$ as the Reynolds number was varied from 990 to 7100; no consistent trend with Reynolds number was found in the experiments. The model agrees with the data when $R_m = 1000$, but shows Reynolds-number dependence. The model's Reynolds-number dependence is as might be expected, and indeed is what Subramanian & Antonia found for $\overline{u^2}$ and $\overline{\theta^2}$: as R_m increases, the peak moves toward

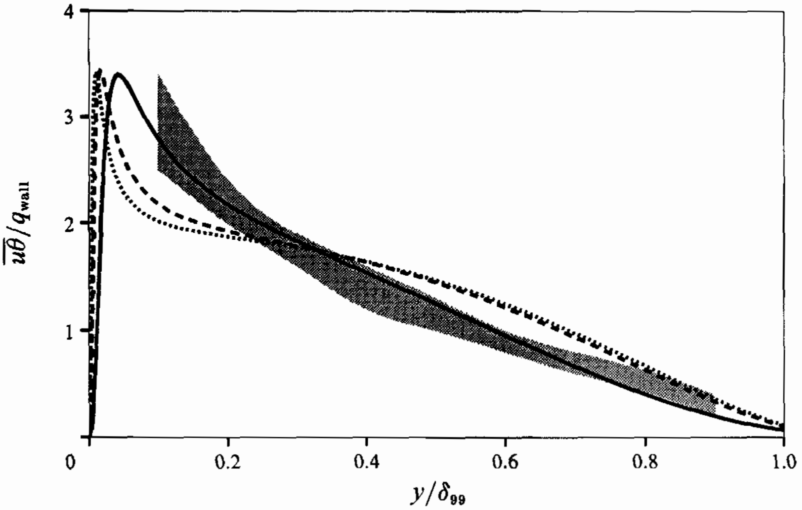

FIGURE 19. Data of Subramanian & Antonia on $\overline{u\theta}$ is shown by shaded region. Model solution: $R_m = 1000$ ——; $R_m = 3000$ ---; $R_m = 5000$….

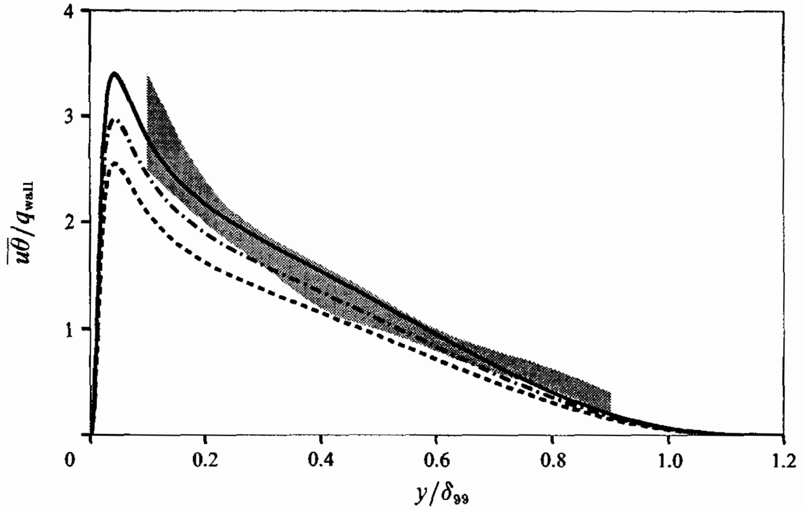

FIGURE 20. Variation of the model solution with C_{θ_3} at $R_m = 1000$. $C_{\theta_3} = 0$ ——; $C_{\theta_3} = 0.2$ —·—; $C_{\theta_3} = 0.4$ ---.

the wall and a knee develops in the log-layer. Because the $\overline{u\theta}$-correlation coefficient is approximately constant and equal to 0.8, and because both u' and θ' profiles develop the near-wall peak and knee, the data on $\overline{u\theta}$ are rather inexplicable. If C_{θ_3} is increased above zero $\overline{u\theta}$ decreases but retains the same R_m dependence as in figure 19. The variation of the model solution with C_{θ_3} is illustrated in figure 20 in which the solid, dash-dot and dashed lines are for $C_{\theta_3} = 0$, 0.2 and 0.4, respectively and $R_m = 1000$; $C_{\theta_3} = 0$ seem to give the most satisfactory agreement to the data.

(iii) As a further estimate of the constants, the model equations can be solved for homogeneously shear turbulence. In this case Reynolds stresses eventually grow exponentially with time, t as $e^{\gamma \mathscr{S} t}$ where $\mathscr{S}$ is the rate of shear and γ is a constant. The ratios of Reynolds stresses reach constant values at large $\mathscr{S}t$. When the present heat-flux model is solved for homogeneous shear, with a uniform mean temperature gradient in the direction of shear, one finds

$$\frac{-\overline{u\theta}}{\overline{v\theta}} = \frac{-\overline{uv}}{\overline{v^2}} + \frac{1-C_{\theta_3}}{\gamma + C_{\theta_1}/\mathscr{S}T} \tag{31}$$

in the exponentially growing regime. This provides a relation between C_{θ_1} and C_{θ_3} if experimental values are given to all other quantities. Tavoularis & Karnik (1989, table 2) summarize various experiments on homogeneously sheared turbulence. Equating t to x/U_c in the experiments allows one to estimate the parameters in (31). An average of the high-shear experiments gives $\gamma = 0.10 \pm 0.016$, where the $\pm$ is the standard deviation of the tabulated values. The table also gives $\mathscr{S}T = 4.1 \pm 0.5$ and $-\overline{uv}/k = 0.32 \pm 0.02$, $\overline{v^2}/k = 0.44 \pm 0.04$ are cited. Substituting these values into (31) with $C_{\theta_1} = 2.5$ and $C_{\theta_3} = 0$ gives 2.14 for the right-hand side. Tavoularis & Corrsin (1981, table 4) give 2.11, 2.17 and 2.22 for $-\overline{u\theta}/\overline{v\theta}$ at three successive downstream locations. Although these do not indicate a clear self-preserving flux ratio, they indicate that the present model constants are roughly in agreement with the data.

Summarizing, the model constants have been determined as follows: the considerations under (ii) suggest $C_{\theta_3} = 0$; the considerations under (iii) then give $C_{\theta_1} = 2.5$; and finally the considerations under (i) imply $C_{\theta_2} = 0.45$. In fact, leeway exists in the estimation of these constants. The present values were also selected on the basis of the curved-wall heat-transfer measurements.

The mean temperature equation in polar coordinates (and $\Psi - x$ variables) is

$$U\partial_x \Theta = \kappa \partial_y^2 \Theta - \partial_y(\alpha\overline{v\theta}) \tag{32}$$

and with the heat-transfer model, (26) becomes

$$\left.\begin{aligned} \frac{U}{\alpha}\partial_x \overline{u\theta} &= (C_{\theta_2}-1)\,\overline{uv}\,\partial_y \Theta - \frac{\overline{v\theta}}{\alpha}\partial_y(\alpha U) - \frac{C_{\theta_1}\epsilon}{k}\overline{u\theta} + \frac{\kappa+\nu}{2}\partial_y^2 \overline{u\theta} + \frac{1}{\alpha}\partial_y(\alpha\nu_{\mathrm{T}_{22}}\partial_y \overline{u\theta}), \\ \frac{U}{\alpha}\partial_x \overline{v\theta} &= (C_{\theta_2}-1)\,\overline{v^2}\,\partial_y \Theta + 2\overline{u\theta}\frac{U}{\alpha R_c} - \frac{C_{\theta_1}\epsilon}{k}\overline{v\theta} + \frac{\kappa+\nu}{2}\partial_y^2 \overline{v\theta} + \frac{1}{\alpha}\partial_y(\alpha\nu_{\mathrm{T}_{22}}\partial_y \overline{v\theta}) \end{aligned}\right\} \tag{33}$$

by analogy with (21) and (22). Figure 21 shows a computation, similar to figure 12, of St/St_0 versus R_m compared to the data from Simon *et al.* (1982). In the curved section the model agrees with the data. In the downstream region the model again predicts too rapid recovery. The recovery of St in figure 21 is slightly faster than the recovery of C_f in figure 12. This is in part because the return to isotropy timescale is T/C_{θ_1} in (29) and T/C_1 in (11). Because $C_{\theta_1} = 2.5$ and $C_1 = 1.22$ the timescale is shorter for the heat-flux equation. It might be noted that 2.5 is on the low side of values typically used for C_{θ_1} (Launder 1978).

6.1. *Discussion of heat-flux model*

The model (29) is a commonly used form; however, it is usual to omit the term with coefficient C_{θ_2} and choose $C_{\theta_3} > 0$ (Launder 1989). The reasoning behind this is based on separating $\overline{\theta\partial_i p}$ into 'rapid' and 'slow' parts. The present approach is more heuristic and is based primarily on considerations (i)–(iii) above. The use of (i) is certainly troubling because $Pr_T \approx 1$ is only suitable for boundary layers, so it is likely that C_{θ_1} or C_{θ_2} would have to vary with flow conditions. At present we are unaware of a more sound approach to heat flux modelling.

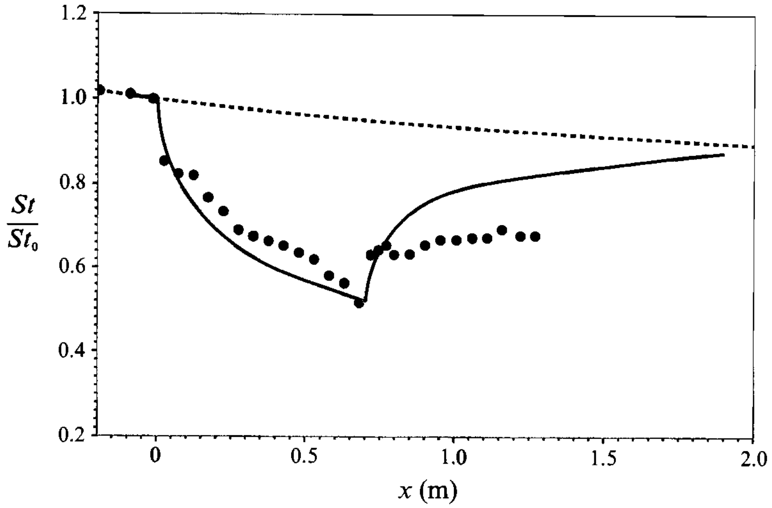

FIGURE 21. Solid line is Stanton number, normalized on its value at the start of curvature; dashed line is normalized Stanton number computed for a flat-plate boundary layer. Data from Simon *et al.* (●).

A further source for some dissatisfaction with the present heat-flux model is that it does not enable boundary conditions to be satisfied. It has already been explained that the representation of kinematic blocking of $\overline{v^2}$ largely ameliorates this shortcoming; but it could, under some circumstances, be cause for concern.

The small-y behaviour of the present Reynolds stress model is analysed in Durbin (1991). That reference shows how the elliptic relaxation model enables boundary conditions on the components of the Reynolds stress tensor to be satisfied. As $y \to 0$ in the heat-flux balance (26), the diffusion and dissipation terms become dominant. The dissipation terms are incorporated into $\wp_{\theta_i}$. Substituting the behaviour $k \to \epsilon y^2/2\nu$ into (26) and (29), the balance between diffusion and dissipation becomes

$$\frac{\kappa+\nu}{2\nu} \partial_y^2 \overline{u_i \theta} = 2C_{\theta_1} \frac{\overline{u_i \theta}}{y^2} + O(y).$$

The non-singular solution to this is $\overline{u_i \theta} = A_i y^n + O(y^3)$ where

$$n = \tfrac{1}{2}\{1 + [1 + 16\nu C_{\theta_1}/(\kappa+\nu)]^{\frac{1}{2}}\}.$$

This equals 2.6 for $C_{\theta_1} = 2.5$ and $\nu/\kappa = 0.71$. The exact behaviour of $\overline{u_i \theta}$ near a constant-temperature boundary is $\overline{u\theta} \propto y^2$ and $\overline{v\theta} \propto y^3$; next to a constant-heat flux boundary $\overline{u\theta} \propto y$ and $\overline{v\theta} \propto y^2$. The limiting behaviour as $y \to 0$ of the present model is not far from correct for boundary layers in air. It is noted in Durbin (1991) that the model equations would probably have to be made fourth order to satisfy the exact boundary conditions.

7. Discussion

The present model was formulated as a coordinate-system-invariant set of equations for the turbulent Reynolds stress tensor. These equations were solved with boundary conditions applied at the surface. Profiles of mean flow and of turbulence statistics were computed directly, by solving the governing equations. Arbitrary functions of y_+

and/or of the turbulence Reynolds number were not used to modify these solutions, or to damp the pressure–strain term; nor were source terms interior to the fluid made to depend on the unit wall normal. Reynolds-number dependence arose naturally from the exact viscous terms; no additional explicit Reynolds-number dependence was introduced into model constants. In all these respects the present model differs from previous near-wall second-order closure models.

Empiricism enters the model only through a small set of constants: in this respect the present formulation is in the spirit of previous models for homogeneous turbulence and free-shear flows. The ability to make use of empiricism in this manner is a necessary and desirable property of turbulence models. The models present an extremely simplified view of turbulence physics, but can make useful predictions by relying on a limited amount of simple and reliable experimental data.

Some of the present model constants have been set to widely used values; others were chosen by comparing the model to data and making adjustments – in the present case the DNS channel flow at $R_\tau = 395$ was used for this purpose. However, the shapes of profiles in figure 1 are produced by properties of the equations, the model constants could be chosen to produce only a few points of quantitative agreement. After the constants were selected on the basis of the channel flow comparison, no further adjustments were made.

The values of the empirical constants, and other aspects of the model, are clearly tailored to the problem of near-wall flow. However, away from surfaces the present model reduces to a standard quasi-homogeneous form; we have used the Rotta return to isotropy plus isotropization of production formulae, but any similar model could have been used.

The strong non-homogeneity of the near-wall region was modelled by the elliptic relaxation equation. This model was motivated by the need to represent non-local effects of the boundary. The computations of zero-pressure-gradient, adverse-pressure-gradient, and convexly curved boundary layers provide an assessment of the model; the focus in that assessment is on the near-wall portion of the boundary layers. The ability of the model to predict the experimental data was quite satisfactory. For example, the skin-friction, displacement-thickness and near-wall behaviour of Reynolds shear stress were predicted quite well for the Samuel & Joubert (1974) experiment. Rodi & Scheurer (1986), and others, have shown how damping-function models are unable to predict this flow.

The most serious deficiency found in the present comparisons was an overprediction of the rate of recovery from convex curvature. This error in the rate of relaxation from perturbation occurs in other situations, such as the recovery from a strong adverse pressure gradient in a downstream region of zero pressure gradient. It seems that this deficiency is associated with inadequacies in the gradient diffusion representation of turbulent self-transport.

I am grateful to Professor P. Moin for his comments on the manuscript.

Appendix A. Rationalization for the elliptic relaxation equation

Justifications for the elliptic model were given by Durbin (1991). Here we will paraphrase one such justification. Consider the Poisson equation for the 'rapid pressure':

$$\nabla^2 p = -2\rho\, \partial_i U_j\, \partial_j u_i. \tag{A 1}$$

Its free-space solution is $$\frac{p}{\rho} = \frac{1}{2\pi}\int \frac{\partial_i U_j(x')\,\partial_j u_i(x')}{|x-x'|}\,\mathrm{d}x'. \tag{A 2}$$

The pressure–velocity gradient correlation is then

$$\overline{p\,\partial_k u_l}(x) = \frac{\rho}{2\pi}\int \frac{\partial_i U_j(x')\,\overline{\partial_j u_i(x')\,\partial_k u_l(x)}}{|x-x'|}\,\mathrm{d}x'. \tag{A 3}$$

The usual quasi-homogeneous approximation involves taking $\partial_i U_j$ outside the integral. Near the wall this term varies rapidly and the quasi-homogeneous approximation is erroneous (Bradshaw *et al.* 1987). An alternative is needed. Suppose instead that the two-point correlation can be represented by an exponential:

$$\overline{\partial_j u_i(x')\,\partial_k u_l\,(x)} \approx \overline{\partial_j u_i\,\partial_k u_l}\,(x')\,\mathrm{e}^{-|x-x'|/L}.$$

Then (A 3) becomes

$$\overline{p\,\partial_k u_l}(x) = \frac{\rho}{2\pi}\int \partial_i U_j(x')\,\overline{\partial_j u_i\,\partial_k u_l}(x')\,\frac{\mathrm{e}^{-|x-x'|L}}{|x-x'|}\,\mathrm{d}x'.$$

This is the solution to $$\left(\nabla^2-\frac{1}{L^2}\right)\overline{p\,\partial_k u_l} = \rho\,\partial_i U_j\,\overline{\partial_j u_i\,\partial_k u_l}, \tag{A 4}$$

which is a template for the present elliptic relaxation equation (8). Note that in practice the exponential correlation and $1/r$ free-space Green's function are not used; rather, the elliptic equation is solved with suitable boundary conditions and variable L.

Appendix B. Transformation of equations to curvilinear coordinates

This appendix explains the method for transforming the model equations to curvilinear coordinates. The transformation was performed *ab initio* on the model equations to assure that the model used here is identical for the planar and curvilinear boundary layers.

The turbulence model is in a tensorally consistent form. To make it coordinate-system independent, one need only recognize the velocity as a contravariant tensor and derivatives as covariant. The equations can then be written in any coordinate system by using differential geometry (McConnell 1957) to project the equations onto the local coordinate directions. It is common practice to rewrite the transformed equations in terms of 'physical components' (Appendix to McConnell 1957). For instance, in plane polar coordinates, the covariant angular velocity is $\mathrm{d}\phi/\mathrm{d}t$ while the physical component is $r\mathrm{d}\phi/\mathrm{d}t$, which has the dimensions of velocity. If $[g_{ij}]$ is the covariant metric tensor, then the physical components of a tensor are obtained by multiplying it by a factor $g^{\frac{1}{2}}_{\alpha\alpha}$ for each contravariant index, α, and dividing by $g^{\frac{1}{2}}_{\beta\beta}$ for each covariant index, β. The convention here is that repeated Greek indices are not summed. Physical components are not tensors. All velocities and derivatives in this paper are considered to be physical components.

The physical components of covariant derivatives are determined by adding a curvature term to a partial derivative:

$$u_{i;j} = \partial_j u_i + \gamma^i_{jk}\,u_k, \tag{B 1}$$

where the semi-colon denotes covariant differentiation (transformed to physical components). Similarly, for a second-order tensor

$$\overline{u_i u_j}_{;k} = \partial_k\,\overline{u_i u_j} + \gamma^i_{kl}\,\overline{u_l u_j} + \gamma^j_{kl}\,\overline{u_i u_l}, \tag{B 2}$$

and so on for higher-order tensors. Operationally, transformation of equations from Cartesian to curvilinear coordinates simply requires consistent substitution of rules like (B 1) and (B 2) in place of partial derivatives. γ^i_{jk} is determined as follows. The contravariant velocity is $u_\alpha/g^{\frac{1}{2}}_{\alpha\alpha}$ (this is simply the inverse of the transformation to physical components). Similarly the covariant derivative of the contravariant velocity is $g^{\frac{1}{2}}_{\beta\beta}(u_\alpha/g^{\frac{1}{2}}_{\alpha\alpha})_{;\beta}$. This is a tensor. According to the above prescription, the physical components of this tensor are $(g_{\alpha\alpha}/g_{\beta\beta})^{\frac{1}{2}}$ times the tensor (it has one covariant index and one contravariant index). Hence

$$\begin{aligned} u_{\alpha;\beta} &\equiv \left(\frac{g_{\alpha\alpha}}{g_{\beta\beta}}\right)^{\frac{1}{2}}\left[g^{\frac{1}{2}}_{\beta\beta}\left(\frac{u_\alpha}{g^{\frac{1}{2}}_{\alpha\alpha}}\right)_{;\beta}\right] \\ &= \left(\frac{g_{\alpha\alpha}}{g_{\beta\beta}}\right)^{\frac{1}{2}}\left[g^{\frac{1}{2}}_{\beta\beta}\,\partial_\beta\left(\frac{u_\alpha}{g^{\frac{1}{2}}_{\alpha\alpha}}\right)+\Gamma^\alpha_{\beta i}\frac{u_i}{g^{\frac{1}{2}}_{ii}}\right]. \end{aligned} \tag{B 3}$$

The bracketed term is a tensor, so $\Gamma^\alpha_{\beta i}$ is the usual Christoffel symbol (McConnell 1957). Comparing (B 3) to (B 1) shows that

$$\gamma^\alpha_{\beta\gamma} = \left(\frac{g_{\alpha\alpha}}{g_{\beta\beta}g_{\gamma\gamma}}\right)^{\frac{1}{2}}\Gamma^\alpha_{\beta\gamma} - \frac{1}{2}\frac{\partial_\beta g_{\alpha\alpha}}{g_{\alpha\alpha}}\delta_{\alpha\gamma}. \tag{B 4}$$

$\gamma^\alpha_{\beta\gamma}$ is not symmetric in its subscripts, unlike $\Gamma^\alpha_{\beta\gamma}$.

For an orthogonal coordinate system $[\boldsymbol{g}]$ is diagonal, $g_{\alpha\beta} = h^2_\alpha\delta_{\alpha\beta}$. For example, in plane polar coordinates with $\mathrm{d}x_1 = r\,\mathrm{d}\phi$ and $\mathrm{d}x_2 = \mathrm{d}r$, $g_{11} = r^2$ and $g_{22} = 1$. (These $g_{\alpha\alpha}$ are by definition the coefficients in the formula $\mathrm{d}l^2 = r^2\,\mathrm{d}\phi^2+\mathrm{d}r^2$.) The physical components of the metric tensor are $G_{\alpha\beta} = g_{\alpha\beta}/(g_{\alpha\alpha}g_{\beta\beta})^{\frac{1}{2}}$. For a diagonal metric $G_{\alpha\beta} = \delta_{\alpha\beta}$. Because $[\boldsymbol{G}]$ interconverts covariant and contravariant components, in orthogonal coordinates there is no need to distinguish covariant and contravariant physical components.

McConnell (1957, appendix eq. 5) gives formulae for Γ^i_{jk} in terms of h_i (note, however, that our h are inverse to his because ours are defined by the covariant metric tensor, and his by the contravariant metric tensor). From these and (B 4) γ^i_{jk} is zero if all i, j and k are all different or all the same, and if i and k are the same. The only non-zero components are

$$\gamma^\alpha_{\alpha\beta} = -\gamma^\beta_{\alpha\alpha} = \frac{1}{h_\alpha}\partial_\beta h_\alpha, \tag{B 5}$$

$\alpha \neq \beta$. For example, in plane polar coordinates $\gamma^1_{12} = -\gamma^2_{11} = 1/r$ and all other components are zero.

The equations in the text were obtained by substituting physical components of covariant derivatives in place of the partial derivatives in the equations of §2, using rules like (B 1) and (B 2) to make the curvature terms explicit, then substituting (B 5) for the case of plane polar coordinates. The only omission of terms in the text is from the turbulent, eddy transport model – given that the equations are in boundary layer form. The exact model is (with $\sigma_k = 1$ for simplicity)

$$(\nu_{T_{kl}}\overline{u_i u_{j;l}})_{;k} = \partial_2(\nu_{T_{2l}}\overline{u_i u_{j;l}})+\gamma^k_{kn}\,\nu_{T_{nl}}\overline{u_i u_{j;l}}+\gamma^i_{kn}\,\nu_{T_{kl}}\overline{u_n u_{j;l}}+\gamma^j_{kn}\,\nu_{T_{kl}}\overline{u_i u_{n;l}} \tag{B 6}$$

in which the boundary-layer approximation justifies ignoring x_1-derivatives. For plane polar coordinates $\gamma^k_{kn} = \delta_{2n}/r$, r being the x_2-direction. Hence, the first two terms in (B 6) can be combined to $(1/r)\,\partial_r(r\nu_{T_{2l}}\overline{u_i u_{j;l}})$. Equation (B 6) shows explicitly how the outermost covariant derivative is expanded; the same procedure must be repeated on the remaining derivatives. The net result is

$$\left.\begin{aligned}
(\nu_{T_{kl}}\overline{u^2}_{;l})_{;k} &= \frac{1}{r}\partial_r(r\nu_{T_{22}}\partial_r\overline{u^2})+\frac{2}{r}\partial_r(\nu_{T_{12}}\overline{uv})+\frac{2\nu_{T_{12}}}{r}\partial_r\overline{uv}+\frac{2}{r^2}\nu_{T_{11}}(\overline{v^2}-\overline{u^2}),\\
(\nu_{T_{kl}}\overline{v^2}_{;l})_{;k} &= \frac{1}{r}\partial_r(r\nu_{T_{22}}\partial_r\overline{v^2})-\frac{2}{r}\partial_r(\nu_{T_{12}}\overline{uv})-\frac{2\nu_{T_{12}}}{r}\partial_r\overline{uv}-\frac{2}{r^2}\nu_{T_{11}}(\overline{v^2}-\overline{u^2}),\\
(\nu_{T_{kl}}\overline{uv}_{;l})_{;k} &= \frac{1}{r}\partial_r(r\nu_{T_{22}}\partial_r\overline{uv})+\frac{1}{r}\partial_r(\nu_{T_{12}}(\overline{v^2}-\overline{u^2}))+\frac{\nu_{T_{12}}}{r}\partial_r(\overline{v^2}-\overline{u^2})-\frac{4}{r^2}\nu_{T_{11}}\overline{uv},
\end{aligned}\right\}\quad\text{(B 7)}$$

in component form. In the text all terms except the first in each equation were omitted: this was done on the grounds that the omitted term are small when $(\delta/R_c) \ll 1$. Numerical computations with these terms included showed them indeed to be small. Their omission simplified the formulation of a stable numerical scheme.

REFERENCES

ALVING, A. E., SMITS, A. J. & WATMUFF, J. H. 1990 Turbulent boundary layer relaxation from convex curvature. *J. Fluid Mech.* **211**, 529–556.

BANDYOPADHYAY, P. R. & AHMED, A. 1993 Turbulent boundary layers subject to multiple curvatures and pressure gradients. *J. Fluid Mech.* **246**, 503–527.

BRADSHAW, P. 1973 The effect of streamline curvature on turbulent flow. *AGARDograph* 169.

BRADSHAW, P., MANSOUR, N. N. & PIOMELLI, U. 1987 On local approximations of the pressure–strain term in turbulence models. *Proc. Summer Program, Center for Turbulence Research, Stanford, University.*

BUSHNELL, D. M. 1983 Turbulent drag reduction. *AIAA Paper* 83-0227.

COLES, D. E. & HIRST, E. A. (eds.) 1968 *Computation of Turbulent Boundary Layers*, vol. 2. AFOSR-IFP-Stanford Conference.

DAKOS, T. & GIBSON, M. M. 1987 On modelling the pressure terms of the scalar flux equations. *Turbulent Shear Flows 5* (ed. F. Durst *et al.*), pp. 7–18. Springer.

DURBIN, P. A. 1991 Near-wall turbulence modeling without damping functions. *Theoret. Comput. Fluid Dyn.* **3**, 1–13.

DURBIN, P. A. 1992 Application of a near-wall turbulence model to boundary layers and heat transfer. *CTR Manuscript* **132**.

DURBIN, P. A. & SPEZIALE, C. G. 1991 Local anisotropy in strained turbulence at high Reynolds number. *Trans. ASME* I: *J. Fluids Engng* **113**, 707–709.

GILLIS, J. C., JOHNSTON, J. P., KAYS, W. M. & MOFFATT, R. J. 1980 Turbulent boundary layer on a convex curved surface. *HMT*-31. Department of Mechanical Engineering, Stanford University.

HANJALIC, K. & LAUNDER, B. E. 1976 Contribution towards a Reynolds-stress closure for low-Reynolds-number turbulence. *J. Fluid Mech.* **74**, 593–610.

HUNT, J. C. R. & GRAHAM, J. M. R. 1978 Free-stream turbulence near plane boundaries. *J. Fluid Mech.* **212**, 497–532.

JOHNSTON, J. P. 1978 Internal Flows. In *Turbulence* (ed. P. Bradshaw). Topics in Applied Physics, vol. 12. Springer.

KLINE, S. J., MORKOVIN, M. V., SOVRAN, G. & COCKRELL, D. J. (eds.) 1968 *Computation of Turbulent Boundary Layers*, vol. 1. AFOSR-IFP-Stanford Conference.

KLEBANOFF, S. 1955 Characteristics of turbulence in a boundary layer with zero pressure gradient. *NACA Rep.* 1247.

LAUNDER, B. E. 1978 Heat and Mass Transport. In *Turbulence* (ed. P. Bradshaw). Topics in Applied Physics, vol. 12. Springer.

LAUNDER, B. E. 1989 Second-moment closure: present... and future. *Intl J. Heat Fluid Flow* **10**, 282–300.

LUMLEY, J. L. & NEWMAN, G. R. 1977 Return to isotropy of homogeneous turbulence. *J. Fluid Mech.* **82**, 161–178.

MANSOUR, N. N., KIM, J. & MOIN, P. 1988 Reynolds-stress and dissipation budgets in a turbulent channel flow. *J. Fluid Mech.* **194**, 15–44.

MCCONNELL, A. J. 1957 *Applications of Tensor Analysis*. Dover.

PATEL, V. C., RODI, W. & SCHEURER, G. 1985 Turbulence models for near-wall and low Reynolds number flows: a review. *AIAA J.* **23**, 1308–1319.

REYNOLDS, W. C., KAYS, W. M. & KLINE, S. J. 1958 Heat transfer in the turbulent incompressible boundary layer. *NACA Memo.* 12-1-58w.

RODI, W. & SCHEURER, G. 1986 Scrutinizing the k–ϵ model under adverse pressure gradient conditions. *Trans. ASME* I: *J. Fluids Engng* **108**, 174–180.

SAMUEL, A. E. & JOUBERT, P. N. 1974 A boundary layer developing in an increasingly adverse pressure gradient. *J. Fluid Mech.* **66**, 481–505.

SCHUBAUER, G. B. & SPANGENBERG, W. G. 1960 Forced mixing in boundary layers. *J. Fluid Mech.* **8**, 10–32.

SIMON, T. W., MOFFATT, R. J., JOHNSTON, J. P. & KAYS, W. M. 1982 Turbulent boundary layer heat transfer experiments: curvature effects including introduction and recovery. *NASA CR* 3510.

SO, R. M. C. & MELLOR, G. L. 1973 Experiment on convex curvature effects in turbulent boundary layers. *J. Fluid Mech.* **60**, 43–62.

SPALART, P. R. 1988 Direct simulation of a turbulent boundary layer up to $R_\theta = 1410$. *J. Fluid Mech.* **187**, 61–98.

SUBRAMANIAN, C. S. & ANTONIA, R. A. 1981 Effect of Reynolds number on a slightly heated turbulent boundary layer. *Intl J. Heat Mass Transfer* **24**, 1833–1846.

TAVOULARIS, S. & CORRSIN, S. 1981 Experiments in nearly homogeneous turbulent shear flow with a uniform mean temperature gradient. Part 1. *J. Fluid Mech.* **104**, 311–347.

TAVOULARIS, S. & KARNIK, U. 1989 Further experiments on the evolution of turbulent stresses and scales in uniformly sheared turbulence. *J. Fluid Mech.* **204**, 457–478.